



Spectra of Cosmic-Ray Sodium and Aluminum and Unexpected Aluminum Excess

M. J. Boschini^{1,2} , S. Della Torre¹ , M. Gervasi^{1,3} , D. Grandi^{1,3} , G. Jóhannesson^{4,5} , G. La Vacca^{1,3} , N. Masi^{6,7} , I. V. Moskalenko^{8,9} , S. Pensotti^{1,3}, T. A. Porter^{8,9} , L. Quadrani^{6,7}, P. G. Rancoita¹ , D. Rozza¹ , and M. Tacconi^{1,3}

¹ INFN, Milano-Bicocca, Milano, Italy

² CINECA, Segrate, Milano, Italy

³ Physics Department, University of Milano-Bicocca, Milano, Italy

⁴ Science Institute, University of Iceland, Dunhaga 3, IS-107 Reykjavik, Iceland

⁵ NORDITA, Roslagstullsbacken 23, SE-106 91 Stockholm, Sweden

⁶ INFN, Bologna, Italy

⁷ Physics Department, University of Bologna, Bologna, Italy

⁸ Hansen Experimental Physics Laboratory, Stanford University, Stanford, CA 94305, USA

⁹ Kavli Institute for Particle Astrophysics and Cosmology, Stanford University, Stanford, CA 94305, USA

Received 2022 February 20; revised 2022 May 1; accepted 2022 May 15; published 2022 July 11

Abstract

Since its launch, the Alpha Magnetic Spectrometer-02 (AMS-02) has delivered outstanding quality measurements of the spectra of cosmic-ray (CR) species, \bar{p} , e^\pm , and nuclei (H–Si, Fe), which resulted in a number of breakthroughs. The most recent AMS-02 result is the measurement of the spectra of CR sodium and aluminum up to ~ 2 TV. Given their low solar system abundances, a significant fraction of each element is produced in fragmentations of heavier species, predominantly Ne, Mg, and Si. In this paper, we use precise measurements of the sodium and aluminum spectra by AMS-02 together with ACE-CRIS and Voyager 1 data to test their origin. We show that the sodium spectrum agrees well with the predictions made with the GALPROP-HELMOD framework, while the aluminum spectrum shows a significant excess in the rigidity range from 2–7 GV. In this context, we discuss the origin of other low-energy excesses in Li, F, and Fe found earlier. The observed excesses in Li, F, and Al appear to be consistent with the local Wolf-Rayet stars hypothesis, invoked to reproduce anomalous $^{22}\text{Ne}/^{20}\text{Ne}$, $^{12}\text{C}/^{16}\text{O}$, and $^{58}\text{Fe}/^{56}\text{Fe}$ ratios in CRs, while excess in Fe is likely connected with a past supernova activity in the solar neighborhood. We also provide updated local interstellar spectra (LIS) of sodium and aluminum in the rigidity range from a few megavolts to ~ 2 TV. Our calculations employ the self-consistent GALPROP-HELMOD framework, which has proved to be a reliable tool in deriving the LIS of CR \bar{p} , e^- , and nuclei $Z \leq 28$.

Unified Astronomy Thesaurus concepts: Galactic cosmic rays (567); Secondary cosmic rays (1438); Heliosphere (711); Interstellar medium (847); Interplanetary medium (825); Galaxy abundances (574)

Supporting material: machine-readable tables

1. Introduction

Precise data at low and high energies delivered by the modern space instrumentation have triggered a number of discoveries of new features in the spectra of cosmic-ray (CR) species enabling unprecedented probes of the stellar nucleosynthesis, properties of the interstellar medium (ISM), and the origin of CRs. A combination of data from individual spacecraft can be combined to cover the enormous range of rigidities, from a few megavolts to tens of teravolts, where the individual spectra of CR species are shaped by many different processes.

With their latest paper on CR sodium and aluminum, the AMS-02 Collaboration (Aguilar et al. 2021b) has now completed their series of papers on CR species H–Si and Fe (Aguilar et al. 2014, 2015a, 2015b, 2016a, 2016b, 2017, 2018a, 2018b, 2019a, 2019b, 2020, 2021b, 2021c, 2021d). Fluorine, sodium, and aluminum in CRs share some common features: all three have odd atomic numbers, and are mostly represented by a single stable isotope with an odd number of nucleons, ^{19}F , ^{23}Na , ^{27}Al , while long-lived radioactive ^{26}Al is present in CRs only fractionally. Because of the properties of

stellar nucleosynthesis, the source and CR abundances of these elements are considerably lower than their even-Z neighbors, ^{16}O , ^{20}Ne , ^{24}Mg , and ^{28}Si . A significant fraction of each element, F, Na, and Al, is produced through the fragmentation of their more abundant neighbors, Ne, Mg, and Si. A comparison of the spectra of F, Na, and Al, and their common and distinct features, may provide new insights into the origin of these elements.

In this paper, we analyze the new CR measurements of the spectra of Na and Al and test their consistency with measurements of other species. We also provide updated Na and Al local interstellar spectra (LIS) in the rigidity range from a few megavolts to ~ 2 TV. Our calculations and interpretation employ the GALPROP¹⁰-HELMOD¹¹ framework that is proved to be a reliable tool in deriving the LIS of CR species (Boschini et al. 2019, 2020a).

2. Calculations

In this work, we use the same CR propagation model with distributed reacceleration and convection that was used in our previous analyses (for more details see Boschini et al. 2017, 2018a, 2018b, 2020a, 2020b, 2021, 2022). The latest



Original content from this work may be used under the terms of the [Creative Commons Attribution 4.0 licence](#). Any further distribution of this work must maintain attribution to the author(s) and the title of the work, journal citation and DOI.

¹⁰ Available from <http://galprop.stanford.edu>.

¹¹ <http://www.helmod.org/>

Table 1
Best-fit Propagation Parameters for I and P scenarios

Parameter	Units	Best Value	Error
z_h	kpc	4.0	0.6
$D_0(R = 4 \text{ GV})$	$\text{cm}^2 \text{ s}^{-1}$	4.3×10^{28}	0.7
δ^a		0.415	0.025
V_{Alf}	km s^{-1}	30	3
dV_{conv}/dz	$\text{km s}^{-1} \text{ kpc}^{-1}$	9.8	0.8

Note.

^a The P scenario assumes a break in the diffusion coefficient with index $\delta_1 = \delta$ below the break and index $\delta_2 = 0.15 \pm 0.03$ above the break at $R = 370 \pm 25$ GV (for details see Boschini et al. 2020b).

version 57 of the GALPROP code for Galactic propagation of CRs and diffuse emissions is described in detail in Porter et al. (2021), see also Boschini et al. (2020a) and references therein.

Full details of the latest HELMOD code version 4 for heliospheric propagation are provided in Boschini et al. (2019). It solves the Fokker–Planck equation for heliospheric propagation in Kolmogorov formulation backward in time (Bobik et al. 2016). The accuracy of the solution was tested using the Crank–Nicholson technique and found to be better than 0.5% at low rigidities. The large number of simulated events ensures that the statistical errors are negligible compared to the other modeling uncertainties.

When comparing our calculations with data collected over an extended period of time, variations in the solar activity are addressed in the following way. The propagation equation is solved for each Carrington rotation, and the numerical results are then combined accordingly to the instrument exposure and the time period. This approach is equivalent to the application of a weighted average that accounts for both exposure time and absolute counting rate variations.

The values of the propagation parameters in the ISM along with their confidence limits are derived from the best available CR data using the Markov Chain Monte Carlo (MCMC) method. Here we use the same method as described in Boschini et al. (2017). Five main propagation parameters, that affect the overall shape of CR spectra, were left free in the scan using GALPROP running in 2D mode: the Galactic halo half width z_h , the normalization of the diffusion coefficient D_0 at the reference rigidity $R = 4$ GV and the index of its rigidity dependence δ , the Alfvén velocity V_{Alf} , and the gradient of the convection velocity dV_{conv}/dz ($V_{\text{conv}} = 0$ in the plane, $z = 0$). Their best-fit values tuned to the AMS-02 data are listed in Table 1 and are the same as obtained in Boschini et al. (2020a). The radial size of the Galaxy does not significantly affect the values of the propagation parameters and was set to 20 kpc. We also introduced a factor β^η in the diffusion coefficient, where $\beta = v/c$, and η was left free. The best-fit value of $\eta = 0.70$ improves the agreement at low energies, and slightly affects the choice of injection indices γ_0 and γ_1 . A detailed discussion of the injection (I) and propagation (P) scenarios of the 350 GV break can be found in the works by Vladimirov et al. (2012) and Boschini et al. (2020a).

The corresponding B/C ratio also remains the same (see Figure 4 of Boschini et al. 2020a), and compares well with all available measurements: Voyager 1 (Cummings et al. 2016), ACE-CRIS¹² (Lave et al. 2013), AMS-02 (Aguilar et al. 2018b), ATIC-2

(Panov et al. 2009), CREAM (Ahn et al. 2008, 2009), and NUCLEON (Grebnyuk et al. 2019).

In the calculations, we use our standard formalism. The convection velocity is assumed to increase linearly with distance z from the plane, $V_{\text{conv}}(z) = V_0 + z \cdot dV_{\text{conv}}/dz$. The spatial diffusion coefficient is parameterized as $D_{xx} = \beta D_0 R^\delta$, where $\beta = v/c$ is the particle velocity. If reacceleration is included, the momentum-space diffusion coefficient D_{pp} is related to D_{xx} as $D_{pp} = p^2 V_{\text{Alf}}^2 / (9D_{xx})$ (Berezinskii et al. 1990; Seo & Ptuskin 1994). See also a review by Strong et al. (2007) and our papers cited at the beginning of this section. The injection spectra of CR species are parameterized by the rigidity-dependent function:

$$q(R) \propto (R/R_0)^{-\gamma_0} \prod_{i=0}^2 [1 + (R/R_i)^{\frac{\gamma_i - \gamma_{i+1}}{s_i}}]^{s_i}, \quad (1)$$

where $\gamma_{i=0,1,2}$ are the spectral indices, $R_{i=0,1,2}$ are the break rigidities, and s_i are the smoothing parameters (s_i is negative/positive for $|\gamma_i| \leq |\gamma_{i+1}|$).

3. Results and Discussion

Figure 1 shows a comparison of the calculated spectrum with Voyager 1 (Cummings et al. 2016), ACE-CRIS (Lave et al. 2013), HEAO-3-C2 (Engelmann et al. 1990), and AMS-02 sodium data (Aguilar et al. 2021d). The calculated spectrum reproduces the data in the whole energy range from 100 MV–2 TV quite well, although there is an insignificant 1σ excess below 7 GV. The injection spectrum of primary sodium is adjusted to the AMS-02 data (Table 2), but remains similar to other species (Boschini et al. 2020a).

Figure 2 shows the calculated Na/F and Na/Si ratios as compared with Voyager 1 (Cummings et al. 2016), ACE-CRIS (Lave et al. 2013), and AMS-02 data (Aguilar et al. 2020, 2021b, 2021d). In the left panel, the dashed gray line shows the default LIS Na/F ratio (with non-renormalized fluorine spectrum), while the solid gray line shows the ratio for the renormalized ($\times 0.896$) fluorine spectrum (for details see Boschini et al. 2022). The solid gray line in the right panel shows the LIS Na/Si ratio. In both panels, the modulated ratios are shown by solid black lines. The Voyager 1 and ACE-CRIS data are converted from kinetic energy per nucleon to rigidity (assuming $A/Z = 2$ for Si). These data are shown as shaded areas with the width corresponding to a 1σ error. Note that the ACE-CRIS data taken during the consequent solar minima overlap.

The ratios, Na/F for renormalized fluorine and Na/Si, exhibit a good overall agreement with the data. There is some discrepancy in the calculated Na/Si ratio with the AMS-02 data at 2–5 GV, which corresponds to $\approx 1\sigma$ (5%) if we take into account the uncertainties in the modulated ratio shown by the gray band. This can be due to the errors in the production cross sections, which we discuss in Section 4. At lower energies, there is a discrepancy with the Voyager 1 data where the Na/Si ratio shows a concave shape, while the calculated ratio shows a monotonic decrease toward the lower energies. This discrepancy is related to large fluctuations (well above the experimental error bars) of the Voyager 1 data points for sodium (see Figure 8 in Boschini et al. 2020a).

Figure 3 shows a comparison of the calculated Al spectra with Voyager 1 (Cummings et al. 2016), ACE-CRIS (Lave et al. 2013), HEAO-3-C2 (Engelmann et al. 1990), and AMS-02 data

¹² http://www.srl.caltech.edu/ACE/ASC/level2/cris_l2desc.html

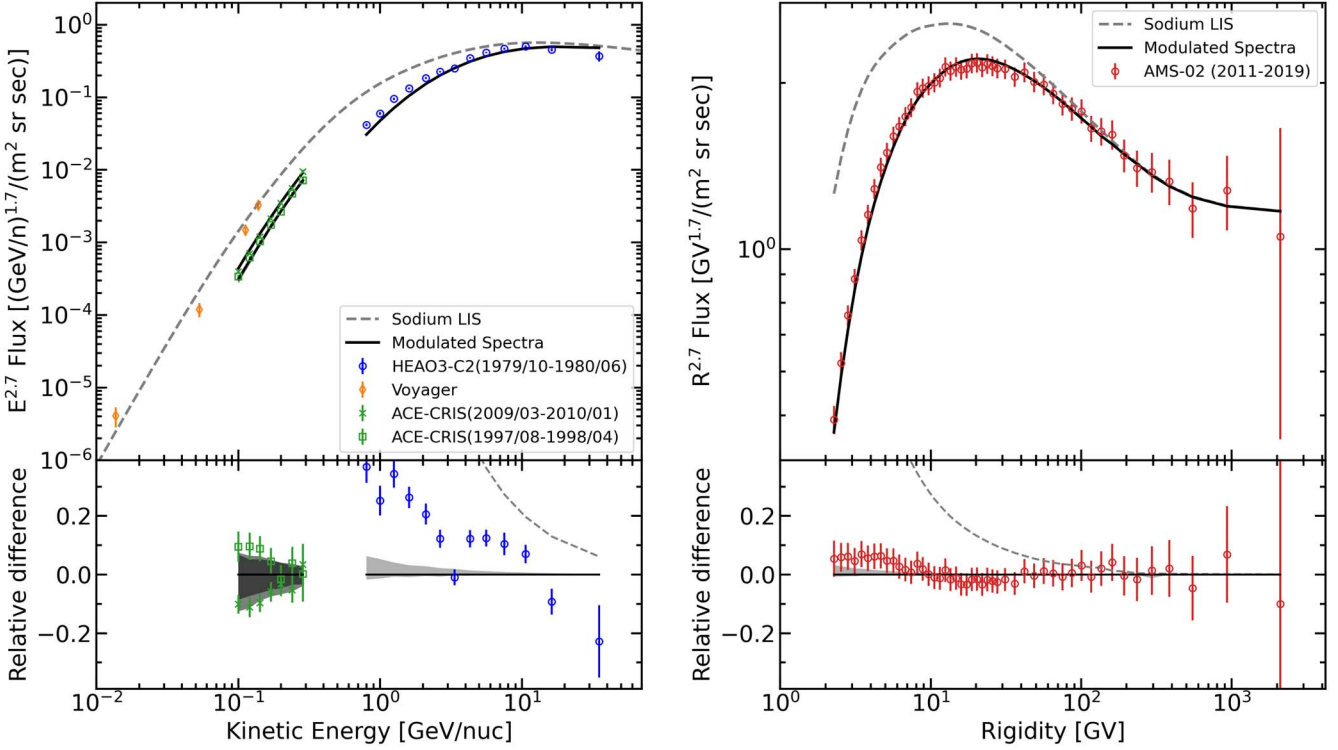


Figure 1. A comparison of the calculated spectrum of sodium with Voyager 1 (Cummings et al. 2016), ACE-CRIS (Lave et al. 2013), HEAO-3-C2 (Engelmann et al. 1990) (left panel), and AMS-02 data (Aguilar et al. 2021d) (right panel). In the left panel, to match the units of the published data, the spectra are plotted vs. kinetic energy per nucleon, E_{kin} . The dashed gray lines show the LIS, and the solid black lines represent the corresponding modulated spectra. The lower panels show the relative difference between our calculations and the data sets. The gray shaded areas indicate 1σ confidence limits for the calculated modulated spectra.

Table 2
The Injection Spectra of Primary Sodium and Aluminum and Aluminum Excess

Source	Abundance	Spectral Parameters										
		γ_0	R_0 (GV)	s_0	γ_1	R_1 (GV)	s_1	γ_2	R_2 (GV)	s_2	γ_3	
²³ Na	default	50	0.24	0.92	0.22	2.33	8.2	0.20	2.49	350	0.16	2.15
²⁷ Al	default	94	0.20	0.60	0.17	2.04	7.0	0.20	2.46	355	0.17	1.93
²⁷ Al	excess	11.5	-5.00	4.0	0.30	5.00

Note. The source abundances are relative, see Table 3 in Boschini et al. (2020a). For parameter definitions see Equation (1). Shown are $|s_i|$ values, note that s_i is negative/positive for $|\gamma_i| \leq |\gamma_{i+1}|$.

(This table is available in machine-readable form.)

(Aguilar et al. 2021d). The top panels show the calculations for a default Al injection spectrum (Table 2, Boschini et al. 2020a), which is slightly adjusted to reproduce AMS-02 data at the highest energies (Table 2). In the top left panel, the Al spectrum is tuned to Voyager 1, ACE-CRIS, and the middle range of the HEAO-3-C2 instrument. The lower and higher energy HEAO-3-C2 data points are biased as was shown in Boschini et al. (2020a), and therefore we did not use them in our fits. To match the units of the published data, the spectra in the left panels are plotted versus kinetic energy per nucleon, E_{kin} . Obvious is a significant excess in the rigidity range of 2–7 GV when compared with AMS-02 data, but outside of this range the agreement is good (Figure 3, top right).

The bottom panels show calculations with a low-energy primary excess component added to the default injection spectrum (see Table 2); its shape was tuned to match the AMS-02 data after propagation. The modified Al spectrum now has a

clear bump, but the agreement with AMS-02 data is significantly improved at the cost of fine-tuning the injection spectrum. Possible reasons for the aluminum excess and other excesses are discussed in Section 4.

Figure 4 shows the calculated Al/F and Al/Si ratios as compared with Voyager 1 (Cummings et al. 2016), ACE-CRIS (Lave et al. 2013), and AMS-02 data (Aguilar et al. 2020, 2021b, 2021d). The Voyager 1 and ACE-CRIS data are converted from kinetic energy per nucleon to rigidity (assuming $A/Z = 2$ for Si). These data are shown as shaded areas with the width corresponding to a 1σ error. The ACE-CRIS data taken during the consequent solar minima are overlapping in the plots. In all panels, the solid gray line shows the corresponding LIS ratio, while the modulated ratios are shown with solid black lines. The top panels show calculations for a default Al injection spectrum (Table 2); in the left panel the ratio with the renormalized ($\times 0.896$) fluorine spectrum is

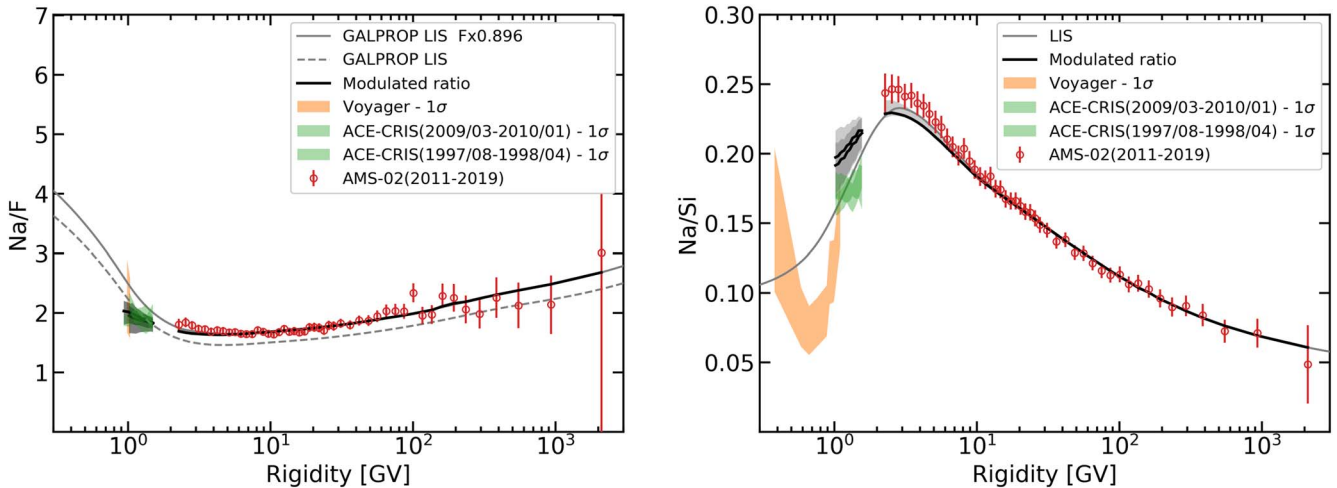


Figure 2. The calculated Na/F and Na/Si ratios as compared with Voyager 1 (Cummings et al. 2016), ACE-CRIS (Lave et al. 2013), and AMS-02 data (Aguilar et al. 2020, 2021b, 2021d). In the left panel, the dashed gray line shows the default LIS Na/F ratio, while the solid gray line shows the ratio for the renormalized ($\times 0.896$) fluorine spectrum (for details see Boschini et al. 2022). The solid gray line in the right panel shows the LIS Na/Si ratio. In both panels, the modulated ratios are shown as solid black lines. The gray shaded areas indicate 1σ confidence limits for the calculated modulated ratios. The Voyager 1 and ACE-CRIS data are converted from kinetic energy per nucleon to rigidity (assuming $A/Z = 2$ for Si). These data are shown as shaded areas with the width corresponding to a 1σ error.

shown (for details see Boschini et al. 2022). Again, one can see a significant excess in the rigidity range of 2–7 GV, while outside of this range the agreement with the data is good. The bottom panels show calculations with a low-energy primary excess component (see Table 2 and Figure 3 bottom) added to the default injection spectrum. For comparison, the dashed gray lines show the default LIS ratios. Again, an additional low-energy component significantly improves the agreement with the data.

The radioactive ^{26}Al isotope in the CR is entirely secondary. Therefore, it provides an independent test of the propagation model and our tuned Al spectrum. The calculated isotopic ratio $^{26}\text{Al}/^{27}\text{Al}$ is compared with available CR data in Figure 5. In the top right panel, we also show the $^{10}\text{Be}/^{9}\text{Be}$ ratio calculated for the same propagation parameters (Table 1). The bottom panels show both ratios calculated for a larger halo size $z_h = 6$ kpc with the adjusted normalization of the spatial diffusion coefficient $D_0(R = 4 \text{ GV}) = 7.5 \times 10^{28} \text{ cm}^2 \text{ s}^{-1}$.

The calculated LIS and modulated ratios are compared with the most precise CR isotopic data available: Voyager 1, 2 data (Lukasiak et al. 1994) collected over a period of 16 yr (1977–1993) as the spacecraft moved from 1 to 53 au and 41 au, correspondingly, Ulysses (Simpson & Connell 1998) and ACE-CRIS (Yanasak et al. 2001). In the plots, the colored symbols show the original published data from different instruments, while the same symbols plotted in black show our predictions based on the calculated LIS. The gray area marks the 1σ error for our predictions.

One can see that the agreement with Voyager 1, 2 and Ulysses data in the top left panel ($^{26}\text{Al}/^{27}\text{Al}$) is good, while the discrepancy with ACE-CRIS data reaches 3σ – 4σ (green squares versus the shaded area with black squares). The increase in the halo size to $z_h = 6$ kpc improves the agreement to $\sim 1\sigma$ for all data sets (bottom left). The $^{10}\text{Be}/^{9}\text{Be}$ ratio agrees well with available data in both cases, $z_h = 4, 6$ kpc.

The difference in the halo size as derived from different radioactive clocks is a well-known issue (Moskalenko et al.

2001, 2005), where the halo size derived from the $^{10}\text{Be}/^{9}\text{Be}$ ratio is systematically lower ($z_h = 1.5$ – 6 kpc) than that derived from other ratios, $^{26}\text{Al}/^{27}\text{Al}$, $^{36}\text{Cl}/\text{Cl}$, $^{54}\text{Mn}/\text{Mn}$; meanwhile, the $z_h = 4$ – 6 kpc range was found to be consistent with all ratios. We note that calculations in Moskalenko et al. (2001, 2005) were done using the force-field approximation and the CR data available at that time.

Overall, the agreement of the calculated $^{10}\text{Be}/^{9}\text{Be}$ and $^{26}\text{Al}/^{27}\text{Al}$ ratio with the data is good (Figure 5), but indicates that halo size limits perhaps have to be reassessed based on new CR data and advances in the treatment of the heliospheric modulation. On the other hand, we emphasize that the production cross sections for Be isotopes are better known than that for isotopes of Al, Cl, and Mn, and this has to be taken into account in a new assessment.

In the Appendix, we provide analytical parameterizations of the Na and default Al LIS, Equations (A1) and (A2), and the total Al LIS, Equation (A3), which also includes the additional primary component. The parameters are provided in Tables 3–5, correspondingly. We also provide numerical tables for all three cases, which tabulate the Na LIS (Tables 6 and 7) and Al LIS (Tables 8 and 9) in rigidity R and in kinetic energy E_{kin} per nucleon, and corresponding Tables 10 and 11 for the total Al LIS, which also includes the additional primary component.

4. Low-energy Excesses in Lithium, Fluorine, Aluminum, and Iron

In this section, we are speculating on the physical reasons for the observed low-energy excess in the aluminum spectrum in the context of other excesses that were found in recent CR data. We do not discuss here the possibility of instrumental errors as they are rather unlikely.

The AMS-02 detector, with its multiple redundancies, provides state-of-the-art measurements of the CR species (Aguilar et al. 2021a). Before its launch, AMS-02 was tested extensively at the CERN test beam with electrons, positrons,

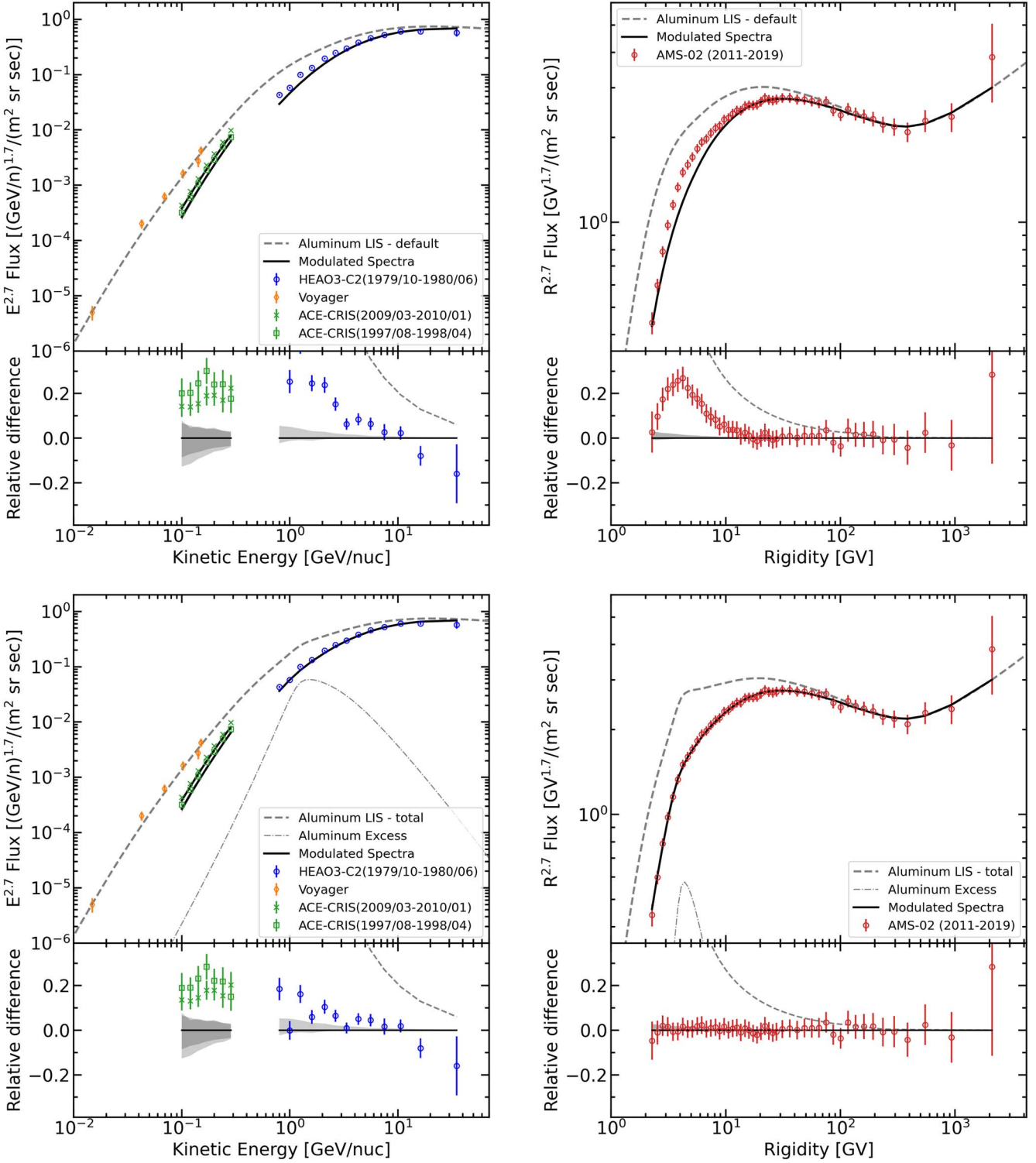


Figure 3. A comparison of the calculated aluminum spectrum with Voyager 1 (Cummings et al. 2016), ACE-CRIS (Lave et al. 2013), HEAO-3-C2 (Engelmann et al. 1990), and AMS-02 data (Aguilar et al. 2021d). The top panels show the calculations made with the default aluminum injection spectrum (Table 2) similar to other Si group species (Table 2, Boschini et al. 2020a). The bottom panels show the total LIS (default+excess), with the injection spectrum of the aluminum excess (Table 2) tuned to the AMS-02 data. The excess is shown separately by the dashed-dotted gray lines. In the left panels, to match the units of the published data, the spectra are plotted vs. kinetic energy per nucleon, E_{kin} . In all panels, the dashed gray line shows the LIS, and the solid black line represents the corresponding modulated spectrum. The gray shaded areas indicate 1σ confidence limits for the calculated modulated spectrum. The lower panels show the relative difference between our calculations and the data sets.

protons, and pions. During more than 10 yr of AMS-02 construction, a large international group of physicists developed a comprehensive Monte Carlo simulation program for AMS-02.

Importantly, the fragmentation cross sections of CR species inside the instrument are measured by the AMS-02 itself using the silicon tracker layers. The procedure and survival

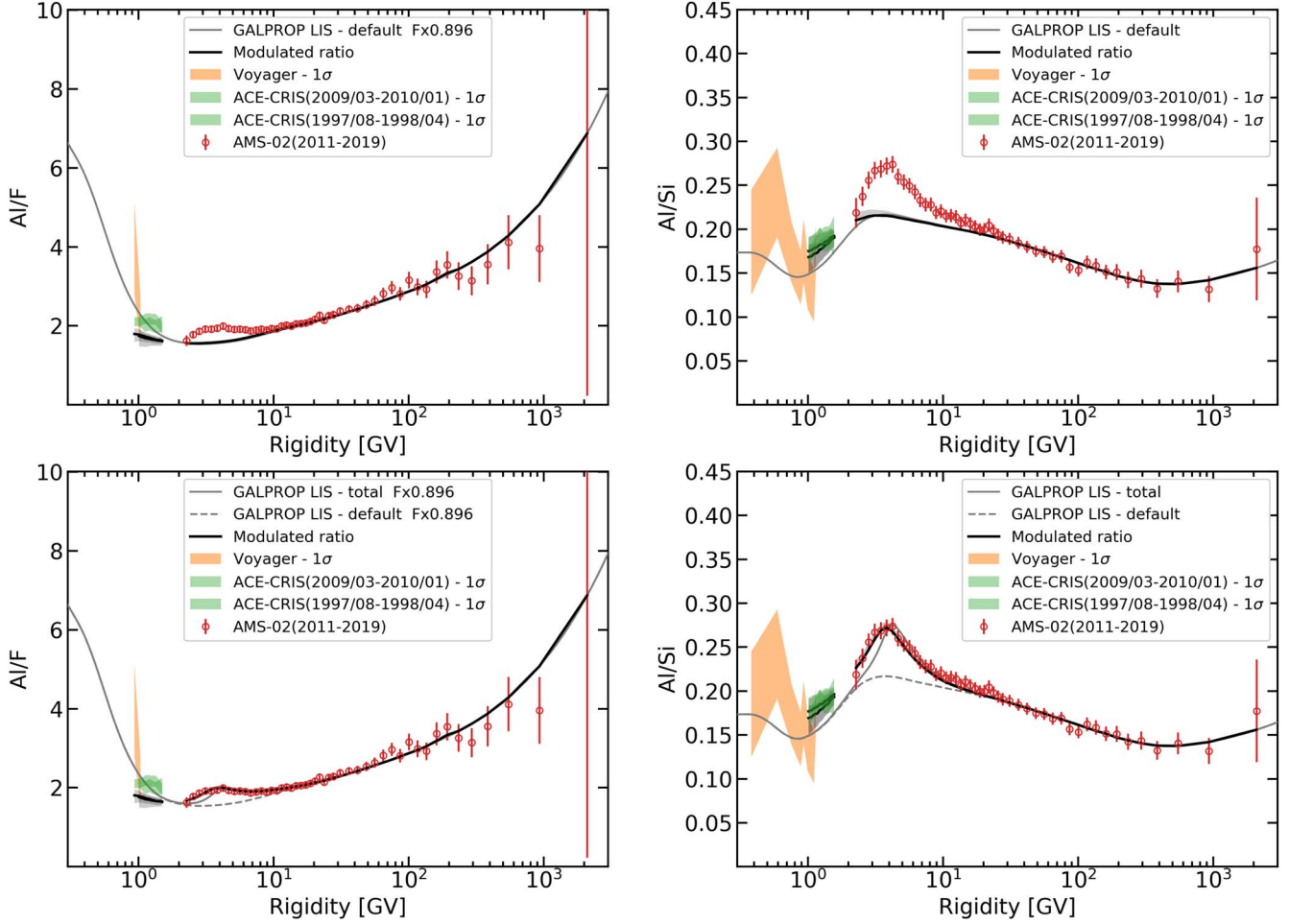


Figure 4. The calculated Al/F and Al/Si ratios as compared with Voyager 1 (Cummings et al. 2016), ACE-CRIS (Lave et al. 2013), HEAO-3-C2 (Engelmann et al. 1990), and AMS-02 data (Aguilar et al. 2020, 2021b, 2021d). In all panels, the solid gray line shows the corresponding LIS ratio, while the modulated ratios are shown by solid black lines. The top panels show calculations for a default Al injection spectrum (Table 2); in the left panel the ratio with the renormalized ($\times 0.896$) fluorine spectrum is shown (for details see Boschini et al. 2022). The bottom panels show calculations with an additional low-energy primary excess component on top of the default injection spectrum. For comparison, the dashed gray lines show the default LIS ratios. The corresponding modulated ratios are shown by the solid black lines. The gray shaded areas indicate 1σ confidence limits for the calculated modulated ratios. The Voyager 1 and ACE-CRIS data are converted from kinetic energy per nucleon to rigidity (assuming $A/Z = 2$ for Si). These data are shown as shaded areas with the width corresponding to a 1σ error.

probabilities for different elements are described in Aguilar et al. (2021a). The data analysis is performed in parallel by several groups, which employ different methods. A good agreement between their results is required before a paper is submitted for publication.

Let us first discuss the default injection spectrum of Al. It is usually assumed that the majority of CR particles are accelerated in supernova remnant (SNR) shocks. The diffusive shock acceleration operating in the shocks as well as the processes in the ISM are insensitive to the nature of particles, while the relevant variable is rigidity. The standard SNR shock acceleration (Malkov & Drury 2001) results in almost identical spectra of injected particles in terms of rigidity. Therefore, the default injection spectrum of Al should be very similar to the spectra of other elements in the Si group, except perhaps at very low energies, which could be sensitive to the local distributions of the ISM gas and CR sources. Table 2 shows the default Al injection spectrum, which is similar to the injection spectra of its neighbors indeed (see Table 2 in Boschini et al. 2020a). There is no viable reason why the Al injection spectrum in the 2–10 GV range should be different from its

neighbors. This led us to conclude that the observed excess must have a different origin, which is discussed below.

There are four possible physical reasons for the observed excess in the Al spectrum: (i) an incorrect spectrum of ^{28}Si , the major progenitor of secondary $^{26,27}\text{Al}$, (ii) errors in the total inelastic cross sections of Al, (iii) errors in the isotopic production cross sections of $^{26,27}\text{Al}$, and (iv) an additional local component of primary Al. Below we discuss them one by one. For completeness, in point (iii) we also discuss the accuracy of the ^{23}Na cross sections. The calculated spectra of Mg and Si, the major progenitors of Na, are tuned to the recent AMS-02 data.

(i) The Si spectrum is tuned to Voyager 1, ACE-CRIS, and AMS-02 data (Boschini et al. 2020a). Importantly, AMS-02 data are available above 2 GV, the same rigidity range for all CR species. This is exactly the energy range where the Al excess is observed. Contributions of other CR species are very minor and cannot be responsible for the observed excess.

(ii) Significant errors in the total inelastic cross section of Al as a primary reason for the excess can be excluded by consideration of the accelerator data. Bobchenko et al. (1979)

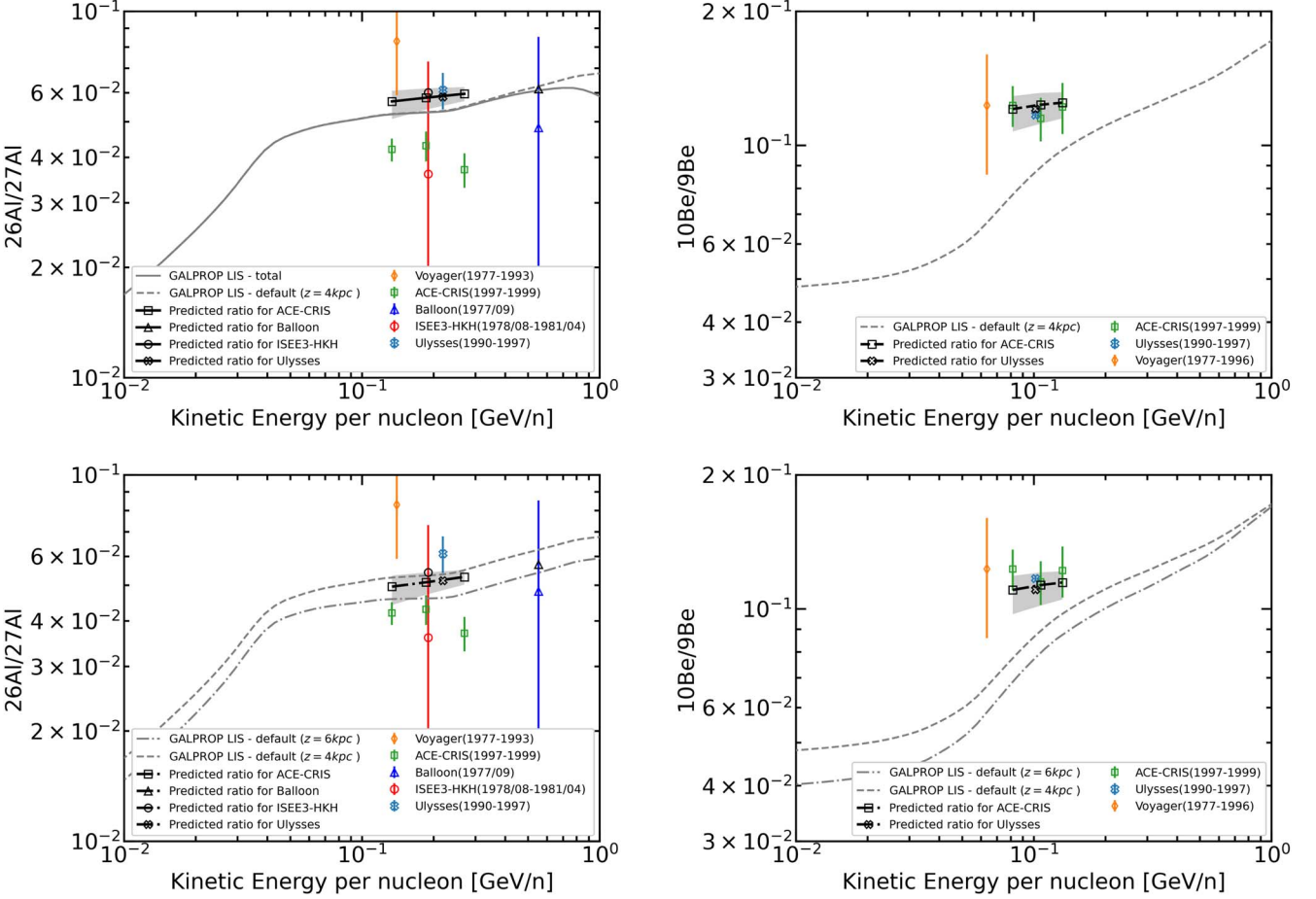


Figure 5. A comparison of the calculated isotopic ratios $^{26}\text{Al}/^{27}\text{Al}$ (left panels) and $^{10}\text{Be}/^{9}\text{Be}$ (right panels) with available data: Voyager 1, 2 data (Lukasiak et al. 1994) collected over a period of 16 yr (1977–1993) in the heliosphere, Ulysses (Simpson & Connell 1998), ACE-CRIS (Yanasak et al. 2001), Balloon (Webber 1982), and ISEE3-HKH (Wiedenbeck 1983). Calculations for the halo size $z_h = 4 are shown in the top panels, and for $z_h = 6 in the bottom panels (with the adjusted normalization of the spatial diffusion coefficient $D_0(R = 4\text{ GV}) = 7.5 \times 10^{-28} \text{ cm}^2 \text{ s}^{-1}$). The dashed gray lines in all plots show the default LIS ratios calculated for $z_h = 4\text{ kpc}$, while the solid gray line in the top left panel shows the LIS ratio with the additional low-energy primary aluminum component. The dashed-dotted lines show the default LIS ratios calculated for $z_h = 6\text{ kpc}$. The colored symbols show the original published data from different instruments, while the same symbols plotted in black show our predictions based on the calculated LIS ratios for $z_h = 4$ (top panels) or 6 kpc (bottom panels). The black line in the gray area shows the modulated ratio, and the gray area marks the 1σ error for our predictions.$$

provide a table of measured proton-nucleus cross sections for the proton momenta from $5\text{--}9\text{ GeV }c^{-1}$, which correspond to the ambient ^{27}Al rigidity range of $10\text{--}19\text{ GV}$ in the inverse kinematics, while the measurement accuracy is stated as being 1%–2%. The average value of the total inelastic cross section in this interval is 456 mb and typical error bars are $\pm 4\text{ mb}$. Most of the data points are consistent with a constant value within the error bars with just four out of a total 17 points being clear outliers at 443 ± 4 , 445 ± 4 , and $467 \pm 4\text{ mb}$ (two points). This is the energy range where the total inelastic cross sections are flat (e.g., see Figure 1 in Wellisch & Axen 1996) and they are easier to measure than the isotopic production. There are also abundant data on the total inelastic cross section of ^{27}Al below $\sim 1\text{ GeV nucleon}^{-1}$ ($< 3\text{ GV}$) (Bauhoff 1986). The parameterizations of the total inelastic cross sections used in our calculations (e.g., Barashenkov & Polanski 1994) are tuned to the available data. That makes a significant error below 7 GV, where the excess is observed, rather unlikely. We note the absence of a similar excess in the spectra of neighboring nuclei, such as Ne, Mg, and Si (Boschini et al. 2020a).

(iii) Almost 100% of secondary ^{27}Al is produced through the fragmentation of ^{28}Si with some minor contributions from ^{29}Si , ^{32}S , and ^{56}Fe (Moskalenko et al. 2013). Unfortunately, the isotopic production cross section $p + ^{28}\text{Si} \rightarrow ^{27}\text{Al}$ is a major source of uncertainty. There are only a couple of measurements available for this reaction: $(E_{\text{kin}}, \sigma) = (218\text{ MeV nucleon}^{-1}, 25\text{ mb})$ (Artun et al. 1975), and $(506\text{ MeV nucleon}^{-1}, 48.5\text{ mb})$ (Webber et al. 1998). These energies correspond to 1.4 and 2.3 GV (^{27}Al) in the inverse kinematics, respectively, and constrain the production of ^{27}Al in the lower range of rigidities where the excess is observed. Clearly, the full energy dependence of the cross section can only be evaluated using semi-phenomenological calculations or nuclear codes (see the description of GALPROP in Boschini et al. 2020a). However, measurements of ^{28}Si fragmentation $^{28}\text{Si} + p \rightarrow \text{Al}$ made by a Siegen group (Hirzebruch et al. 1991) indicate that the cross section remains flat between 1 and $14.5\text{ GeV nucleon}^{-1}$. This energy range corresponds to the rigidity range from 3.5–31 GV (^{27}Al), which covers the excess range and extends to significantly higher rigidities. Therefore, even though the cross

section between ≈ 500 and ≈ 1000 MeV nucleon $^{-1}$ remains unconstrained, it has no effect on the excess, which is observed in the rigidity range of 2–7 GV with the maximum at ≈ 4 GV. The latter corresponds to $E_{\text{kin}} \approx 1.2$ GeV nucleon $^{-1}$, i.e., where the cross section is flat.

To further investigate the issue, we looked at another aluminum isotope, ^{26}Al , which is mostly produced through the fragmentation of ^{28}Si and ^{27}Al (Moskalenko et al. 2013). Since we compare our calculations with the observed CR isotopic ratio $^{26}\text{Al}/^{27}\text{Al}$ below 1 GeV nucleon $^{-1}$ (Figure 5), our concern is the accuracy of the calculations of the production of ^{26}Al in this energy range with a correction for heliospheric modulation. Fortunately, the production of ^{26}Al is well constrained below 1 GeV nucleon $^{-1}$. The experimental data points with references can be found in the EXFOR¹³ database; the data points from different experiments are consistent within the error bars.

The calculated $^{26}\text{Al}/^{27}\text{Al}$ ratio (Figure 5, bottom left, $z_h = 6$ kpc) agrees well with available CR data corrected for the corresponding level of heliospheric modulation. To summarize, it is unlikely that the uncertainties in the production cross sections of $^{26,27}\text{Al}$ can result in the observed excess.

We also comment here on the accuracy of the sodium cross sections. The total inelastic cross section is calculated using the same parameterizations that are used for other species (Barashenkov & Polanski 1994). It should be accurate enough given that the total inelastic cross sections of its neighbors, Ne and Mg, are well measured. The production cross sections of ^{23}Na are less certain. The secondary sodium ^{23}Na is produced through the fragmentation of ^{24}Mg (dominant channel) and ^{28}Si with minor contributions of ^{25}Mg , ^{26}Mg , and ^{27}Al (Moskalenko et al. 2013). Unfortunately, there is only a single measurement for each parent nucleus, $^{24,25,26}\text{Mg}$, ^{28}Si , and ^{27}Al , made by Webber et al. (1990) at the LBL Bevalac using ~ 600 MeV nucleon $^{-1}$ beams. Therefore, we use the updated semi-phenomenological parameterizations by Webber et al. (2003) renormalized to the data. The beam energy of ~ 600 MeV nucleon $^{-1}$ (corresponds to ^{23}Na rigidity of ~ 2.5 GV) above which the expected cross section behavior is quite smooth. It is reasonable to expect that Na production cross sections should be flat above 2.5 GV, i.e., extending into the rigidity range of 2–7 GV of the observed Al excess.

(iv) The observed low-energy excess in the aluminum spectrum is most likely due to the stable isotope ^{27}Al . However, because it is stable, its yield and Galactic distribution are difficult to measure. Meanwhile, abundant literature exists on the observations of the distribution of the diffuse γ -ray 1.809 MeV line emission from the decay of the radioactive ^{26}Al isotope and on its origin. Therefore, we discuss the origin of ^{26}Al assuming that the same sources are producing ^{27}Al as well.

Studies of the primitive meteoritic grains indicate that the early solar system material was enriched with short-lived radionuclides, such as ^{10}Be , ^{26}Al , ^{36}Cl , ^{41}Ca , ^{53}Mn , ^{60}Fe , and others (Goswami et al. 2005). In particular, the presolar meteoritic ratio $^{26}\text{Al}/^{27}\text{Al} \sim 4.5 \times 10^{-5}$ derived from the excess of ^{26}Mg is surprisingly well determined despite the fact that the half-life of ^{26}Al of ~ 700 kyr is much shorter than the formation time of the solar system. Therefore, a local source of ^{26}Al , such as a nearby SN or an AGB star, which injected fresh ^{26}Al into the forming solar system, is usually invoked.

Observations of the distribution of the diffuse Galactic 1.809 MeV γ -ray emission line from ^{26}Al decay by COMPTEL (Diehl et al. 1995; Oberlack et al. 1996; Knölseder et al. 1999) and INTEGRAL (Bouchet et al. 2015) have shown that ^{26}Al nucleosynthesis is ongoing in the present Galaxy. Potential sources include AGB stars, novae, core-collapse supernovae, and Wolf-Rayet (W-R) star winds (Prantzos & Diehl 1996; Diehl et al. 2006). A very recent review of the nucleosynthesis reactions involved in the production and destruction of ^{26}Al and ^{60}Fe and characteristics of the stellar sites of their nucleosynthesis can be found in Diehl et al. (2021).

Apparently, the sources of cosmic Al are numerous, and are simultaneously also the sources of other rare isotopes, such as ^{7}Li , ^{19}F , ^{60}Fe , and others (see discussions in our papers: Boschini et al. 2020b, 2021, 2022, and references therein). Particularly interesting is a possible contribution of the massive W-R stars proposed to explain the observed anomalous $^{22}\text{Ne}/^{20}\text{Ne}$ ratio and other observed ratios, $^{12}\text{C}/^{16}\text{O}$ and $^{58}\text{Fe}/^{56}\text{Fe}$, in CRs (Binns et al. 2008). It was shown that all isotopic ratios measured with ACE-CRIS are consistent with CR source composition consisting of $\sim 20\%$ of W-R material mixed with $\sim 80\%$ material with solar system composition. Since most W-R stars are found in the OB associations and are the evolutionary stages of OB stars, the OB associations (through multiple SN explosions) are the likely sources of a substantial fraction of CRs. W-R stars are also most likely local sources of ^{7}Li and ^{19}F , while ^{60}Fe may come from an SN or a series of SN explosions 1–2 Myr ago in the solar neighborhood (Binns et al. 2016).

Regarding the spectrum of sodium, we note the absence of a similar low-energy excess. An interesting analysis using the Gaia-ESO Survey to study sodium and aluminum abundances in giants and dwarfs and its implications for stellar and Galactic chemical evolution can be found in Smiljanic et al. (2016). W-R stars do not seem to be a significant source of sodium. The absence of the excess in the sodium spectrum apparently supports the hypothesis of the origin of the observed excesses in the local OB associations. Meanwhile, studies of sodium nucleosynthesis in different stellar environments are desirable as they may help to discriminate between possible scenarios of the origin of the observed excesses.

5. Conclusion

Using the combined data of AMS-02 (Aguilar et al. 2021c), ACE-CRIS (Lave et al. 2013), and Voyager 1 (Cummings et al. 2016) we analyzed the spectra of sodium and aluminum over a wide rigidity range from 100 MV up to 2 TV. We found that the sodium spectrum agrees well with the predictions made with the GALPROP-HELMOD framework, while aluminum spectrum shows a significant excess in the rigidity range from 2 to 7 GV.

Our analysis shows that among four possible reasons for the observed excess, a contribution of local sources is most likely. In this context, we discuss the origin of other low-energy excesses in Li, F, and Fe found earlier (Boschini et al. 2020b, 2021, 2022). It seems that the W-R hypothesis that was invoked to reproduce the observed isotopic ratios, $^{22}\text{Ne}/^{20}\text{Ne}$, $^{12}\text{C}/^{16}\text{O}$, $^{58}\text{Fe}/^{56}\text{Fe}$, and other observed CR abundances (Binns et al. 2008) is also consistent with the observed excesses in Li, F, and Al, while excess in Fe may be connected with a past SN activity in the solar neighborhood. The absence of a

¹³ <https://www-nds.iaea.org/exfor/>

corresponding excess in sodium supports this hypothesis, as the W-R winds are not a significant source of sodium.

Finally, we note that the exploration of the low-energy features in the spectra of CR species has just begun, thanks to the data from the interstellar probes Voyager 1, 2, and precise measurements by AMS-02, ACE-CRIS, and other instruments. These features harbor the keys to understanding our local Galactic environment and the history of the formation of the solar system. The increase in the collected statistics and

(Di Felice et al. 2017) and the LPSC Database of Charged Cosmic Rays (Maurin et al. 2014).

Appendix

Analytical Parameterization and Numerical Tables of the Sodium and Aluminum LIS

Here we provide an analytical parameterization of the sodium LIS ($\text{m}^{-2} \text{ sr}^{-1} \text{ s}^{-1} \text{ GV}^{-1}$):

$$F_{\text{Na}}(R) = \begin{cases} a - bR\tilde{R} - G(R)(c + dR - fR^3) - g(hR^4)^{G(R)}, & R \leq 2.8 \text{ GV}, \\ R^{-2.7} \left[-i - lR + m\sqrt{n - \frac{o}{R} + p\sqrt{R}} + qR \tanh\left(-\frac{rR}{sR + R^2 - t\sqrt{R}}\right) \right], & R > 2.8 \text{ GV}, \end{cases} \quad (\text{A1})$$

reduction in the systematic errors will help to establish the precise spectral shapes of observed features and to facilitate their interpretation.

Special thanks to Pavol Bobik, Giuliano Boella, Marian Putis, and Mario Zannoni for their continuous support of the

where R is the particle rigidity in gigavolts, the expressions for \tilde{R} and $G(x)$ are given in Equation (A4), and the values of the fitting parameters from a to z are summarized in Table 3.

We also provide analytical parameterizations of the *default* aluminum LIS and total aluminum LIS (with the excess), units are $\text{m}^{-2} \text{ sr}^{-1} \text{ s}^{-1} \text{ GV}^{-1}$:

$$F_{\text{Al}}^{\text{default}}(R) = \begin{cases} a - \frac{b}{R} + cR^3 + dR^2G(R) - fR^2 - gR G(R) - hG^4(R), & R \leq 3.6 \text{ GV}, \\ R^{-2.7} \left[i\tilde{R} + l\sqrt{R} + \frac{m}{\log(n + oR)} + p \log^2(n + oR) - q - rR\tilde{R} - s\tilde{R}^2 \right], & R > 3.6 \text{ GV}, \end{cases} \quad (\text{A2})$$

$$F_{\text{Al}}^{\text{total}}(R) = \begin{cases} aR + \frac{b}{R} + cR^3 + dR\tilde{R}^4G^2(R) - f - gR^2 - h\tilde{R}^2, & R \leq 3.2 \text{ GV}, \\ R^{-2.7} \{ iR - l + m \tanh(R) + \tilde{R}(n - oR) + p \log(q + R\tilde{R}) - rL[s \log(q + R\tilde{R})] \}, & R > 3.2 \text{ GV}, \end{cases} \quad (\text{A3})$$

HelMod project and many useful suggestions. This work was carried out using THE HELMOD tool, which is currently supported within ASIF-ASI (Agenzia Spaziale Italiana) Supported Irradiation Facilities-framework for space radiation environment activities, e.g., ASIF implementation agreements 2017-22-HD.0 ASI-ENEA, 2017-15-HD.0 ASI-INFN, 2021-39-HH.0 ASI-ENEA and ASIF implementation agreement 2021-36-HH.0 involving ASI and Milano-Bicocca University. This work is also supported by ASI contract ASI-INFN 2019-19-HH.0 and ESA (European Space Agency) contract 4000116146/16/NL/HK. I.V. M. and T.A.P. acknowledge the support from NASA grant Nos. NNX17AB48G, 80NSSC22K0718, and 80NSSC22K0477. This research has made use of the SSDC Cosmic Ray Database

where R is the particle rigidity in gigavolts,

$$\begin{aligned} \tilde{R} &= \log R, \\ G(x) &= e^{-x^2}, \\ L(x) &= 1/(1 + e^{-x}), \end{aligned} \quad (\text{A4})$$

and the values of the fitting parameters from a to z are given in Tables 4 and 5.

The analytical representations, Equations (A1)–(A3), are also complemented by numerical tables calculated for the *I* scenario, which tabulate the LIS in rigidity R (Tables 6, 8, and 10), and in kinetic energy E_{kin} per nucleon (Tables 7, 9, and 11).

Table 3
Parameters of the Analytical Fit to the Sodium LIS, Equation (A1)

Param	Value	Param	Value	Param	Value	Param	Value
<i>a</i>	2.8359e-1	<i>g</i>	9.2254e-2	<i>n</i>	3.3852e+0	<i>s</i>	4.100e+1
<i>b</i>	3.1660e-2	<i>h</i>	1.0122e-1	<i>o</i>	4.0058e+0	<i>t</i>	4.8223e+1
<i>c</i>	2.8544e-1	<i>i</i>	2.9718e+0	<i>p</i>	9.9286e-4
<i>d</i>	7.4636e-2	<i>l</i>	3.3525e-7	<i>q</i>	2.8346e-2
<i>f</i>	1.2551e-1	<i>m</i>	3.3510e+0	<i>r</i>	7.3991e+1

(This table is available in machine-readable form.)

Table 4
Parameters of the Analytical Fit to the *Default* Aluminum LIS, Equation (A2)

Param	Value	Param	Value	Param	Value	Param	Value
<i>a</i>	2.1141e-1	<i>g</i>	2.0344e-1	<i>n</i>	2.7104e+0	<i>s</i>	1.4698e-1
<i>b</i>	9.7044e-4	<i>h</i>	1.8791e-1	<i>o</i>	3.0751e-2
<i>c</i>	4.0776e-3	<i>i</i>	1.8105e+0	<i>p</i>	1.4367e-1
<i>d</i>	1.0513e-1	<i>l</i>	2.2979e-2	<i>q</i>	7.6313e+0
<i>f</i>	2.6449e-2	<i>m</i>	7.4947e+0	<i>r</i>	3.1067e-7

(This table is available in machine-readable form.)

Table 5
Parameters of the Analytical Fit to the Total Aluminum LIS, Equation (A3)

Param	Value	Param	Value	Param	Value	Param	Value
<i>a</i>	2.3066e-1	<i>g</i>	8.9912e-2	<i>n</i>	6.3989e-1	<i>s</i>	2.3391e-1
<i>b</i>	2.4724e-2	<i>h</i>	9.5355e-2	<i>o</i>	8.5007e-6
<i>c</i>	1.2692e-2	<i>i</i>	1.2796e-4	<i>p</i>	1.6380e+0
<i>d</i>	9.6944e-2	<i>l</i>	9.5849e+1	<i>q</i>	1.2755e+2
<i>f</i>	2.9140e-2	<i>m</i>	1.4909e+2	<i>r</i>	7.8534e+1

(This table is available in machine-readable form.)

Table 6
 $Z = 11$ —Sodium LIS

Rigidity GV	Differential Intensity								
9.027e-02	7.982e-04	7.289e-01	1.083e-01	1.008e+01	4.958e-03	5.271e+02	5.598e-08	3.313e+04	7.803e-13
9.473e-02	9.152e-04	7.661e-01	1.167e-01	1.094e+01	3.994e-03	5.802e+02	4.277e-08	3.649e+04	6.047e-13
9.941e-02	1.035e-03	8.054e-01	1.251e-01	1.188e+01	3.206e-03	6.387e+02	3.271e-08	4.018e+04	4.687e-13
1.043e-01	1.171e-03	8.469e-01	1.334e-01	1.292e+01	2.563e-03	7.032e+02	2.504e-08	4.424e+04	3.633e-13
1.095e-01	1.324e-03	8.906e-01	1.413e-01	1.405e+01	2.040e-03	7.741e+02	1.919e-08	4.872e+04	2.817e-13
1.149e-01	1.498e-03	9.369e-01	1.488e-01	1.530e+01	1.617e-03	8.523e+02	1.471e-08	5.365e+04	2.185e-13
1.206e-01	1.694e-03	9.857e-01	1.556e-01	1.668e+01	1.277e-03	9.383e+02	1.129e-08	5.908e+04	1.695e-13
1.265e-01	1.916e-03	1.037e+00	1.619e-01	1.819e+01	1.004e-03	1.033e+03	8.668e-09	6.506e+04	1.315e-13
1.328e-01	2.167e-03	1.092e+00	1.674e-01	1.985e+01	7.862e-04	1.137e+03	6.661e-09	7.164e+04	1.020e-13
1.393e-01	2.451e-03	1.150e+00	1.721e-01	2.168e+01	6.136e-04	1.252e+03	5.122e-09	7.889e+04	7.918e-14
1.462e-01	2.772e-03	1.211e+00	1.760e-01	2.369e+01	4.771e-04	1.379e+03	3.939e-09	8.687e+04	6.146e-14
1.535e-01	3.134e-03	1.276e+00	1.789e-01	2.590e+01	3.696e-04	1.518e+03	3.031e-09	9.566e+04	4.772e-14
1.611e-01	3.543e-03	1.345e+00	1.809e-01	2.834e+01	2.854e-04	1.671e+03	2.333e-09	1.053e+05	3.705e-14
1.690e-01	4.005e-03	1.419e+00	1.816e-01	3.103e+01	2.199e-04	1.840e+03	1.796e-09	1.160e+05	2.878e-14
1.774e-01	4.526e-03	1.497e+00	1.812e-01	3.398e+01	1.690e-04	2.026e+03	1.383e-09	1.277e+05	2.235e-14
1.862e-01	5.114e-03	1.580e+00	1.795e-01	3.723e+01	1.295e-04	2.231e+03	1.066e-09	1.407e+05	1.736e-14
1.954e-01	5.776e-03	1.668e+00	1.764e-01	4.081e+01	9.914e-05	2.457e+03	8.214e-10	1.549e+05	1.349e-14
2.050e-01	6.522e-03	1.763e+00	1.720e-01	4.475e+01	7.572e-05	2.705e+03	6.332e-10	1.706e+05	1.049e-14
2.152e-01	7.362e-03	1.863e+00	1.662e-01	4.909e+01	5.773e-05	2.979e+03	4.883e-10	1.878e+05	8.150e-15
2.259e-01	8.307e-03	1.971e+00	1.592e-01	5.387e+01	4.394e-05	3.280e+03	3.766e-10	2.068e+05	6.335e-15
2.371e-01	9.369e-03	2.087e+00	1.510e-01	5.913e+01	3.340e-05	3.612e+03	2.905e-10
2.488e-01	1.056e-02	2.211e+00	1.419e-01	6.492e+01	2.536e-05	3.977e+03	2.241e-10
2.611e-01	1.190e-02	2.344e+00	1.321e-01	7.130e+01	1.923e-05	4.379e+03	1.729e-10
2.741e-01	1.340e-02	2.487e+00	1.220e-01	7.832e+01	1.457e-05	4.822e+03	1.334e-10
2.877e-01	1.508e-02	2.640e+00	1.115e-01	8.605e+01	1.103e-05	5.310e+03	1.030e-10
3.020e-01	1.695e-02	2.806e+00	1.010e-01	9.457e+01	8.347e-06	5.847e+03	7.952e-11

Table 6
(Continued)

Rigidity GV	Differential Intensity								
3.170e-01	1.905e-02	2.985e+00	9.058e-02	1.039e+02	6.310e-06	6.438e+03	6.140e-11
3.328e-01	2.138e-02	3.179e+00	8.052e-02	1.143e+02	4.766e-06	7.090e+03	4.742e-11
3.493e-01	2.397e-02	3.388e+00	7.097e-02	1.256e+02	3.598e-06	7.807e+03	3.663e-11
3.667e-01	2.686e-02	3.615e+00	6.205e-02	1.382e+02	2.716e-06	8.596e+03	2.830e-11
3.850e-01	3.005e-02	3.862e+00	5.379e-02	1.519e+02	2.050e-06	9.466e+03	2.187e-11
4.042e-01	3.358e-02	4.129e+00	4.627e-02	1.671e+02	1.547e-06	1.042e+04	1.690e-11
4.244e-01	3.748e-02	4.421e+00	3.951e-02	1.838e+02	1.168e-06	1.148e+04	1.307e-11
4.456e-01	4.178e-02	4.738e+00	3.352e-02	2.022e+02	8.820e-07	1.264e+04	1.010e-11
4.679e-01	4.649e-02	5.083e+00	2.831e-02	2.225e+02	6.664e-07	1.392e+04	7.814e-12
4.913e-01	5.163e-02	5.460e+00	2.377e-02	2.448e+02	5.039e-07	1.533e+04	6.045e-12
5.160e-01	5.724e-02	5.872e+00	1.987e-02	2.694e+02	3.813e-07	1.688e+04	4.676e-12
5.419e-01	6.330e-02	6.323e+00	1.654e-02	2.965e+02	2.888e-07	1.858e+04	3.619e-12

Note. Differential intensity units: $(\text{m}^2 \text{ s sr GV})^{-1}$.

(This table is available in machine-readable form.)

Table 7
 $Z = 11$ —Sodium LIS

E_{kin} GeV n^{-1}	Differential Intensity								
1.000e-03	3.605e-02	6.309e-02	6.463e-01	3.981e+00	1.056e-02	2.512e+02	1.170e-07	1.585e+04	1.632e-12
1.101e-03	3.939e-02	6.948e-02	6.668e-01	4.384e+00	8.482e-03	2.766e+02	8.942e-08	1.745e+04	1.264e-12
1.213e-03	4.246e-02	7.651e-02	6.846e-01	4.827e+00	6.793e-03	3.046e+02	6.839e-08	1.922e+04	9.800e-13
1.335e-03	4.577e-02	8.425e-02	6.993e-01	5.315e+00	5.419e-03	3.354e+02	5.236e-08	2.116e+04	7.597e-13
1.470e-03	4.934e-02	9.277e-02	7.104e-01	5.853e+00	4.306e-03	3.693e+02	4.012e-08	2.330e+04	5.891e-13
1.619e-03	5.318e-02	1.022e-01	7.175e-01	6.446e+00	3.408e-03	4.067e+02	3.076e-08	2.566e+04	4.568e-13
1.783e-03	5.733e-02	1.125e-01	7.206e-01	7.098e+00	2.688e-03	4.478e+02	2.361e-08	2.825e+04	3.543e-13
1.963e-03	6.181e-02	1.239e-01	7.199e-01	7.816e+00	2.111e-03	4.931e+02	1.812e-08	3.111e+04	2.749e-13
2.162e-03	6.663e-02	1.364e-01	7.156e-01	8.607e+00	1.652e-03	5.430e+02	1.393e-08	3.426e+04	2.133e-13
2.381e-03	7.182e-02	1.502e-01	7.078e-01	9.478e+00	1.288e-03	5.980e+02	1.071e-08	3.773e+04	1.656e-13
2.622e-03	7.741e-02	1.654e-01	6.968e-01	1.044e+01	1.001e-03	6.585e+02	8.237e-09	4.155e+04	1.285e-13
2.887e-03	8.343e-02	1.822e-01	6.826e-01	1.149e+01	7.750e-04	7.251e+02	6.338e-09	4.575e+04	9.977e-14
3.179e-03	8.990e-02	2.006e-01	6.654e-01	1.266e+01	5.982e-04	7.985e+02	4.878e-09	5.038e+04	7.747e-14
3.501e-03	9.686e-02	2.209e-01	6.450e-01	1.394e+01	4.606e-04	8.793e+02	3.755e-09	5.548e+04	6.017e-14
3.855e-03	1.043e-01	2.432e-01	6.218e-01	1.535e+01	3.538e-04	9.682e+02	2.892e-09	6.109e+04	4.674e-14
4.245e-03	1.124e-01	2.678e-01	5.957e-01	1.690e+01	2.712e-04	1.066e+03	2.228e-09	6.727e+04	3.631e-14
4.675e-03	1.210e-01	2.949e-01	5.671e-01	1.861e+01	2.075e-04	1.174e+03	1.717e-09	7.408e+04	2.821e-14
5.148e-03	1.303e-01	3.248e-01	5.360e-01	2.049e+01	1.585e-04	1.293e+03	1.324e-09	8.157e+04	2.192e-14
5.669e-03	1.402e-01	3.577e-01	5.027e-01	2.257e+01	1.208e-04	1.424e+03	1.021e-09	8.983e+04	1.704e-14
6.242e-03	1.508e-01	3.938e-01	4.679e-01	2.485e+01	9.194e-05	1.568e+03	7.873e-10	9.892e+04	1.325e-14
6.874e-03	1.621e-01	4.337e-01	4.318e-01	2.736e+01	6.988e-05	1.726e+03	6.073e-10
7.569e-03	1.743e-01	4.776e-01	3.953e-01	3.013e+01	5.305e-05	1.901e+03	4.685e-10
8.335e-03	1.872e-01	5.259e-01	3.592e-01	3.318e+01	4.023e-05	2.093e+03	3.615e-10
9.179e-03	2.010e-01	5.791e-01	3.239e-01	3.654e+01	3.048e-05	2.305e+03	2.790e-10
1.011e-02	2.157e-01	6.377e-01	2.897e-01	4.023e+01	2.308e-05	2.539e+03	2.154e-10
1.113e-02	2.313e-01	7.022e-01	2.570e-01	4.431e+01	1.746e-05	2.795e+03	1.663e-10
1.226e-02	2.479e-01	7.733e-01	2.261e-01	4.879e+01	1.320e-05	3.078e+03	1.284e-10
1.350e-02	2.654e-01	8.515e-01	1.974e-01	5.373e+01	9.968e-06	3.390e+03	9.916e-11
1.486e-02	2.840e-01	9.377e-01	1.712e-01	5.916e+01	7.525e-06	3.733e+03	7.660e-11
1.637e-02	3.035e-01	1.033e+00	1.474e-01	6.515e+01	5.679e-06	4.110e+03	5.918e-11
1.802e-02	3.240e-01	1.137e+00	1.260e-01	7.174e+01	4.286e-06	4.526e+03	4.573e-11
1.985e-02	3.456e-01	1.252e+00	1.070e-01	7.900e+01	3.235e-06	4.984e+03	3.535e-11
2.185e-02	3.682e-01	1.379e+00	9.027e-02	8.699e+01	2.442e-06	5.489e+03	2.732e-11
2.406e-02	3.917e-01	1.518e+00	7.579e-02	9.580e+01	1.844e-06	6.044e+03	2.113e-11
2.650e-02	4.161e-01	1.672e+00	6.338e-02	1.055e+02	1.394e-06	6.656e+03	1.634e-11
2.918e-02	4.414e-01	1.841e+00	5.278e-02	1.162e+02	1.054e-06	7.329e+03	1.264e-11
3.213e-02	4.673e-01	2.027e+00	4.378e-02	1.279e+02	7.972e-07	8.071e+03	9.778e-12
3.539e-02	4.938e-01	2.233e+00	3.620e-02	1.409e+02	6.039e-07	8.887e+03	7.567e-12

Note. Differential intensity units: $(\text{m}^2 \text{ s GeV n}^{-1})^{-1}$.

(This table is available in machine-readable form.)

Table 8
 $Z = 13$ —Default Aluminum LIS

Rigidity GV	Differential Intensity								
8.967e-02	1.397e-03	7.240e-01	1.196e-01	1.002e+01	5.553e-03	5.236e+02	1.016e-07	3.291e+04	4.657e-12
9.410e-02	1.595e-03	7.610e-01	1.249e-01	1.087e+01	4.530e-03	5.763e+02	7.925e-08	3.624e+04	3.713e-12
9.875e-02	1.801e-03	8.000e-01	1.299e-01	1.180e+01	3.680e-03	6.345e+02	6.195e-08	3.991e+04	2.961e-12
1.036e-01	2.034e-03	8.412e-01	1.348e-01	1.283e+01	2.975e-03	6.985e+02	4.852e-08	4.395e+04	2.361e-12
1.087e-01	2.296e-03	8.847e-01	1.393e-01	1.396e+01	2.394e-03	7.689e+02	3.807e-08	4.840e+04	1.882e-12
1.141e-01	2.592e-03	9.306e-01	1.435e-01	1.520e+01	1.918e-03	8.466e+02	2.990e-08	5.329e+04	1.501e-12
1.198e-01	2.926e-03	9.791e-01	1.473e-01	1.656e+01	1.530e-03	9.320e+02	2.352e-08	5.868e+04	1.197e-12
1.257e-01	3.302e-03	1.030e+00	1.506e-01	1.806e+01	1.216e-03	1.026e+03	1.852e-08	6.462e+04	9.548e-13
1.319e-01	3.726e-03	1.085e+00	1.534e-01	1.972e+01	9.622e-04	1.130e+03	1.461e-08	7.116e+04	7.615e-13
1.384e-01	4.204e-03	1.142e+00	1.556e-01	2.153e+01	7.589e-04	1.244e+03	1.153e-08	7.836e+04	6.074e-13
1.453e-01	4.742e-03	1.203e+00	1.572e-01	2.353e+01	5.964e-04	1.370e+03	9.105e-09	8.629e+04	4.845e-13
1.524e-01	5.348e-03	1.268e+00	1.582e-01	2.573e+01	4.670e-04	1.508e+03	7.196e-09	9.502e+04	3.865e-13
1.600e-01	6.029e-03	1.336e+00	1.586e-01	2.815e+01	3.646e-04	1.660e+03	5.691e-09	1.046e+05	3.083e-13
1.679e-01	6.795e-03	1.409e+00	1.584e-01	3.082e+01	2.839e-04	1.828e+03	4.503e-09	1.152e+05	2.459e-13
1.762e-01	7.655e-03	1.487e+00	1.578e-01	3.375e+01	2.205e-04	2.013e+03	3.565e-09	1.269e+05	1.962e-13
1.849e-01	8.620e-03	1.569e+00	1.562e-01	3.698e+01	1.709e-04	2.216e+03	2.824e-09	1.397e+05	1.565e-13
1.941e-01	9.703e-03	1.657e+00	1.538e-01	4.054e+01	1.322e-04	2.440e+03	2.239e-09	1.539e+05	1.249e-13
2.037e-01	1.092e-02	1.751e+00	1.504e-01	4.445e+01	1.020e-04	2.687e+03	1.775e-09	1.694e+05	9.962e-14
2.138e-01	1.227e-02	1.851e+00	1.460e-01	4.876e+01	7.861e-05	2.959e+03	1.408e-09	1.866e+05	7.947e-14
2.243e-01	1.379e-02	1.958e+00	1.407e-01	5.351e+01	6.045e-05	3.258e+03	1.117e-09	2.054e+05	6.341e-14
2.355e-01	1.549e-02	2.073e+00	1.344e-01	5.873e+01	4.642e-05	3.588e+03	8.870e-10
2.471e-01	1.738e-02	2.196e+00	1.273e-01	6.449e+01	3.560e-05	3.950e+03	7.043e-10
2.594e-01	1.948e-02	2.328e+00	1.195e-01	7.082e+01	2.727e-05	4.350e+03	5.594e-10
2.723e-01	2.182e-02	2.470e+00	1.111e-01	7.780e+01	2.086e-05	4.790e+03	4.445e-10
2.858e-01	2.442e-02	2.623e+00	1.022e-01	8.548e+01	1.595e-05	5.274e+03	3.533e-10
3.000e-01	2.729e-02	2.788e+00	9.325e-02	9.394e+01	1.218e-05	5.808e+03	2.808e-10
3.149e-01	3.047e-02	2.965e+00	8.441e-02	1.032e+02	9.299e-06	6.395e+03	2.233e-10
3.305e-01	3.397e-02	3.158e+00	7.574e-02	1.135e+02	7.091e-06	7.042e+03	1.776e-10
3.470e-01	3.782e-02	3.366e+00	6.736e-02	1.248e+02	5.404e-06	7.754e+03	1.413e-10
3.642e-01	4.202e-02	3.591e+00	5.940e-02	1.372e+02	4.117e-06	8.539e+03	1.124e-10
3.824e-01	4.657e-02	3.836e+00	5.194e-02	1.509e+02	3.136e-06	9.403e+03	8.946e-11
4.015e-01	5.143e-02	4.102e+00	4.505e-02	1.660e+02	2.389e-06	1.035e+04	7.121e-11
4.215e-01	5.654e-02	4.391e+00	3.880e-02	1.826e+02	1.821e-06	1.140e+04	5.669e-11
4.426e-01	6.191e-02	4.706e+00	3.322e-02	2.009e+02	1.389e-06	1.255e+04	4.514e-11
4.647e-01	6.747e-02	5.049e+00	2.830e-02	2.210e+02	1.060e-06	1.383e+04	3.595e-11
4.880e-01	7.321e-02	5.424e+00	2.400e-02	2.432e+02	8.097e-07	1.522e+04	2.863e-11
5.125e-01	7.907e-02	5.833e+00	2.027e-02	2.676e+02	6.196e-07	1.676e+04	2.281e-11
5.383e-01	8.500e-02	6.280e+00	1.707e-02	2.945e+02	4.750e-07	1.846e+04	1.817e-11

Note. Differential intensity units: $(\text{m}^2 \text{ s sr GV})^{-1}$.

(This table is available in machine-readable form.)

Table 9
 $Z = 13$ —Default Aluminum LIS

E_{kin} GeV n^{-1}	Differential Intensity								
1.000e-03	6.256e-02	6.309e-02	7.060e-01	3.981e+00	1.179e-02	2.512e+02	2.122e-07	1.585e+04	9.680e-12
1.101e-03	6.811e-02	6.948e-02	7.058e-01	4.384e+00	9.592e-03	2.766e+02	1.655e-07	1.745e+04	7.717e-12
1.213e-03	7.329e-02	7.651e-02	7.037e-01	4.827e+00	7.776e-03	3.046e+02	1.294e-07	1.922e+04	6.153e-12
1.335e-03	7.886e-02	8.425e-02	6.996e-01	5.315e+00	6.275e-03	3.354e+02	1.013e-07	2.116e+04	4.906e-12
1.470e-03	8.485e-02	9.277e-02	6.935e-01	5.853e+00	5.042e-03	3.693e+02	7.946e-08	2.330e+04	3.912e-12
1.619e-03	9.128e-02	1.022e-01	6.855e-01	6.446e+00	4.034e-03	4.067e+02	6.241e-08	2.566e+04	3.120e-12
1.783e-03	9.820e-02	1.125e-01	6.756e-01	7.098e+00	3.215e-03	4.478e+02	4.908e-08	2.825e+04	2.488e-12
1.963e-03	1.056e-01	1.239e-01	6.636e-01	7.816e+00	2.552e-03	4.931e+02	3.864e-08	3.111e+04	1.984e-12
2.162e-03	1.136e-01	1.364e-01	6.497e-01	8.607e+00	2.019e-03	5.430e+02	3.047e-08	3.426e+04	1.582e-12
2.381e-03	1.222e-01	1.502e-01	6.340e-01	9.478e+00	1.591e-03	5.980e+02	2.404e-08	3.773e+04	1.262e-12
2.622e-03	1.313e-01	1.654e-01	6.168e-01	1.044e+01	1.250e-03	6.585e+02	1.899e-08	4.155e+04	1.007e-12
2.887e-03	1.412e-01	1.822e-01	5.982e-01	1.149e+01	9.785e-04	7.251e+02	1.500e-08	4.575e+04	8.030e-13
3.179e-03	1.517e-01	2.006e-01	5.785e-01	1.266e+01	7.638e-04	7.985e+02	1.186e-08	5.038e+04	6.405e-13
3.501e-03	1.629e-01	2.209e-01	5.578e-01	1.394e+01	5.946e-04	8.793e+02	9.385e-09	5.548e+04	5.110e-13
3.855e-03	1.750e-01	2.432e-01	5.366e-01	1.535e+01	4.618e-04	9.682e+02	7.429e-09	6.109e+04	4.076e-13

Table 9
(Continued)

E_{kin} GeV n ⁻¹	Differential Intensity								
4.245e-03	1.878e-01	2.678e-01	5.141e-01	1.690e+01	3.579e-04	1.066e+03	5.884e-09	6.727e+04	3.252e-13
4.675e-03	2.015e-01	2.949e-01	4.901e-01	1.861e+01	2.768e-04	1.174e+03	4.664e-09	7.408e+04	2.594e-13
5.148e-03	2.161e-01	3.248e-01	4.647e-01	2.049e+01	2.137e-04	1.293e+03	3.697e-09	8.157e+04	2.070e-13
5.669e-03	2.316e-01	3.577e-01	4.380e-01	2.257e+01	1.646e-04	1.424e+03	2.933e-09	8.983e+04	1.651e-13
6.242e-03	2.481e-01	3.938e-01	4.102e-01	2.485e+01	1.266e-04	1.568e+03	2.327e-09	9.892e+04	1.317e-13
6.874e-03	2.656e-01	4.337e-01	3.816e-01	2.736e+01	9.719e-05	1.726e+03	1.847e-09
7.569e-03	2.841e-01	4.776e-01	3.522e-01	3.013e+01	7.454e-05	1.901e+03	1.466e-09
8.335e-03	3.036e-01	5.259e-01	3.226e-01	3.318e+01	5.709e-05	2.093e+03	1.165e-09
9.179e-03	3.243e-01	5.791e-01	2.931e-01	3.654e+01	4.369e-05	2.305e+03	9.252e-10
1.011e-02	3.460e-01	6.377e-01	2.640e-01	4.023e+01	3.340e-05	2.539e+03	7.352e-10
1.113e-02	3.688e-01	7.022e-01	2.359e-01	4.431e+01	2.551e-05	2.795e+03	5.844e-10
1.226e-02	3.926e-01	7.733e-01	2.096e-01	4.879e+01	1.947e-05	3.078e+03	4.646e-10
1.350e-02	4.175e-01	8.515e-01	1.848e-01	5.373e+01	1.485e-05	3.390e+03	3.695e-10
1.486e-02	4.433e-01	9.377e-01	1.617e-01	5.916e+01	1.131e-05	3.733e+03	2.939e-10
1.637e-02	4.698e-01	1.033e+00	1.405e-01	6.515e+01	8.618e-06	4.110e+03	2.338e-10
1.802e-02	4.968e-01	1.137e+00	1.211e-01	7.174e+01	6.564e-06	4.526e+03	1.861e-10
1.985e-02	5.235e-01	1.252e+00	1.037e-01	7.900e+01	5.001e-06	4.984e+03	1.481e-10
2.185e-02	5.492e-01	1.379e+00	8.831e-02	8.699e+01	3.811e-06	5.489e+03	1.179e-10
2.406e-02	5.738e-01	1.518e+00	7.479e-02	9.580e+01	2.906e-06	6.044e+03	9.387e-11
2.650e-02	5.969e-01	1.672e+00	6.311e-02	1.055e+02	2.217e-06	6.656e+03	7.475e-11
2.918e-02	6.182e-01	1.841e+00	5.306e-02	1.162e+02	1.694e-06	7.329e+03	5.953e-11
3.213e-02	6.376e-01	2.027e+00	4.446e-02	1.279e+02	1.296e-06	8.071e+03	4.742e-11
3.539e-02	6.548e-01	2.233e+00	3.721e-02	1.409e+02	9.936e-07	8.887e+03	3.778e-11

Note. Differential intensity units: (m² s sr GeV n⁻¹)⁻¹.

(This table is available in machine-readable form.)

Table 10
Z = 13—Total Aluminum LIS

Rigidity GV	Differential Intensity								
8.967e-02	1.397e-03	7.240e-01	1.197e-01	1.002e+01	5.812e-03	5.236e+02	1.016e-07	3.291e+04	4.657e-12
9.410e-02	1.596e-03	7.610e-01	1.250e-01	1.087e+01	4.701e-03	5.763e+02	7.925e-08	3.624e+04	3.713e-12
9.875e-02	1.802e-03	8.000e-01	1.301e-01	1.180e+01	3.791e-03	6.345e+02	6.195e-08	3.991e+04	2.961e-12
1.036e-01	2.034e-03	8.412e-01	1.350e-01	1.283e+01	3.047e-03	6.985e+02	4.852e-08	4.395e+04	2.361e-12
1.087e-01	2.297e-03	8.847e-01	1.395e-01	1.396e+01	2.440e-03	7.689e+02	3.807e-08	4.840e+04	1.882e-12
1.141e-01	2.593e-03	9.306e-01	1.438e-01	1.520e+01	1.947e-03	8.466e+02	2.990e-08	5.329e+04	1.501e-12
1.198e-01	2.927e-03	9.791e-01	1.476e-01	1.656e+01	1.549e-03	9.320e+02	2.352e-08	5.868e+04	1.197e-12
1.257e-01	3.303e-03	1.030e+00	1.509e-01	1.806e+01	1.227e-03	1.026e+03	1.852e-08	6.462e+04	9.548e-13
1.319e-01	3.727e-03	1.085e+00	1.537e-01	1.972e+01	9.696e-04	1.130e+03	1.461e-08	7.116e+04	7.615e-13
1.384e-01	4.206e-03	1.142e+00	1.560e-01	2.153e+01	7.635e-04	1.244e+03	1.153e-08	7.836e+04	6.074e-13
1.453e-01	4.744e-03	1.203e+00	1.577e-01	2.353e+01	5.993e-04	1.370e+03	9.105e-09	8.629e+04	4.845e-13
1.524e-01	5.350e-03	1.268e+00	1.588e-01	2.573e+01	4.688e-04	1.508e+03	7.196e-09	9.502e+04	3.865e-13
1.600e-01	6.031e-03	1.336e+00	1.593e-01	2.815e+01	3.657e-04	1.660e+03	5.691e-09	1.046e+05	3.083e-13
1.679e-01	6.797e-03	1.409e+00	1.592e-01	3.082e+01	2.846e-04	1.828e+03	4.503e-09	1.152e+05	2.459e-13
1.762e-01	7.657e-03	1.487e+00	1.586e-01	3.375e+01	2.210e-04	2.013e+03	3.565e-09	1.269e+05	1.962e-13
1.849e-01	8.623e-03	1.569e+00	1.572e-01	3.698e+01	1.712e-04	2.216e+03	2.824e-09	1.397e+05	1.565e-13
1.941e-01	9.706e-03	1.657e+00	1.549e-01	4.054e+01	1.324e-04	2.440e+03	2.239e-09	1.539e+05	1.249e-13
2.037e-01	1.092e-02	1.751e+00	1.517e-01	4.445e+01	1.021e-04	2.687e+03	1.775e-09	1.694e+05	9.962e-14
2.138e-01	1.228e-02	1.851e+00	1.476e-01	4.876e+01	7.867e-05	2.959e+03	1.408e-09	1.866e+05	7.947e-14
2.243e-01	1.380e-02	1.958e+00	1.426e-01	5.351e+01	6.049e-05	3.258e+03	1.117e-09	2.054e+05	6.341e-14
2.355e-01	1.549e-02	2.073e+00	1.367e-01	5.873e+01	4.644e-05	3.588e+03	8.870e-10
2.471e-01	1.738e-02	2.196e+00	1.300e-01	6.449e+01	3.561e-05	3.950e+03	7.043e-10
2.594e-01	1.949e-02	2.328e+00	1.227e-01	7.082e+01	2.728e-05	4.350e+03	5.594e-10
2.723e-01	2.183e-02	2.470e+00	1.150e-01	7.780e+01	2.087e-05	4.790e+03	4.445e-10
2.858e-01	2.443e-02	2.623e+00	1.070e-01	8.548e+01	1.595e-05	5.274e+03	3.533e-10
3.000e-01	2.730e-02	2.788e+00	9.897e-02	9.394e+01	1.219e-05	5.808e+03	2.808e-10
3.149e-01	3.048e-02	2.965e+00	9.132e-02	1.032e+02	9.300e-06	6.395e+03	2.233e-10

Table 10
(Continued)

Rigidity GV	Differential Intensity								
3.305e-01	3.398e-02	3.158e+00	8.404e-02	1.135e+02	7.092e-06	7.042e+03	1.776e-10
3.470e-01	3.783e-02	3.366e+00	7.722e-02	1.248e+02	5.404e-06	7.754e+03	1.413e-10
3.642e-01	4.204e-02	3.591e+00	7.083e-02	1.372e+02	4.117e-06	8.539e+03	1.124e-10
3.824e-01	4.659e-02	3.836e+00	6.448e-02	1.509e+02	3.136e-06	9.403e+03	8.946e-11
4.015e-01	5.146e-02	4.102e+00	5.738e-02	1.660e+02	2.389e-06	1.035e+04	7.121e-11
4.215e-01	5.657e-02	4.391e+00	4.941e-02	1.826e+02	1.821e-06	1.140e+04	5.669e-11
4.426e-01	6.194e-02	4.706e+00	4.167e-02	2.009e+02	1.389e-06	1.255e+04	4.514e-11
4.647e-01	6.750e-02	5.049e+00	3.476e-02	2.210e+02	1.060e-06	1.383e+04	3.595e-11
4.880e-01	7.325e-02	5.424e+00	2.881e-02	2.432e+02	8.097e-07	1.522e+04	2.863e-11
5.125e-01	7.911e-02	5.833e+00	2.378e-02	2.676e+02	6.196e-07	1.676e+04	2.281e-11
5.383e-01	8.505e-02	6.280e+00	1.959e-02	2.945e+02	4.750e-07	1.846e+04	1.817e-11

Note. Differential intensity units: $(m^2 \text{ s sr GV})^{-1}$.

(This table is available in machine-readable form.)

Table 11
 $Z = 13$ —Total Aluminum LIS

E_{kin} GeV n^{-1}	Differential Intensity								
1.000e-03	6.258e-02	6.309e-02	7.068e-01	3.981e+00	1.234e-02	2.512e+02	2.122e-07	1.585e+04	9.680e-12
1.101e-03	6.813e-02	6.948e-02	7.066e-01	4.384e+00	9.952e-03	2.766e+02	1.655e-07	1.745e+04	7.717e-12
1.213e-03	7.331e-02	7.651e-02	7.045e-01	4.827e+00	8.010e-03	3.046e+02	1.294e-07	1.922e+04	6.153e-12
1.335e-03	7.888e-02	8.425e-02	7.005e-01	5.315e+00	6.426e-03	3.354e+02	1.013e-07	2.116e+04	4.906e-12
1.470e-03	8.487e-02	9.277e-02	6.946e-01	5.853e+00	5.138e-03	3.693e+02	7.946e-08	2.330e+04	3.912e-12
1.619e-03	9.131e-02	1.022e-01	6.867e-01	6.446e+00	4.095e-03	4.067e+02	6.241e-08	2.566e+04	3.120e-12
1.783e-03	9.823e-02	1.125e-01	6.768e-01	7.098e+00	3.254e-03	4.478e+02	4.908e-08	2.825e+04	2.488e-12
1.963e-03	1.057e-01	1.239e-01	6.650e-01	7.816e+00	2.577e-03	4.931e+02	3.864e-08	3.111e+04	1.984e-12
2.162e-03	1.136e-01	1.364e-01	6.512e-01	8.607e+00	2.034e-03	5.430e+02	3.047e-08	3.426e+04	1.582e-12
2.381e-03	1.222e-01	1.502e-01	6.357e-01	9.478e+00	1.601e-03	5.980e+02	2.404e-08	3.773e+04	1.262e-12
2.622e-03	1.314e-01	1.654e-01	6.187e-01	1.044e+01	1.256e-03	6.585e+02	1.899e-08	4.155e+04	1.007e-12
2.887e-03	1.412e-01	1.822e-01	6.003e-01	1.149e+01	9.823e-04	7.251e+02	1.500e-08	4.575e+04	8.030e-13
3.179e-03	1.517e-01	2.006e-01	5.808e-01	1.266e+01	7.661e-04	7.985e+02	1.186e-08	5.038e+04	6.405e-13
3.501e-03	1.630e-01	2.209e-01	5.604e-01	1.394e+01	5.961e-04	8.793e+02	9.385e-09	5.548e+04	5.110e-13
3.855e-03	1.750e-01	2.432e-01	5.395e-01	1.535e+01	4.627e-04	9.682e+02	7.429e-09	6.109e+04	4.076e-13
4.245e-03	1.879e-01	2.678e-01	5.174e-01	1.690e+01	3.585e-04	1.066e+03	5.884e-09	6.727e+04	3.252e-13
4.675e-03	2.016e-01	2.949e-01	4.938e-01	1.861e+01	2.772e-04	1.174e+03	4.664e-09	7.408e+04	2.594e-13
5.148e-03	2.162e-01	3.248e-01	4.689e-01	2.049e+01	2.139e-04	1.293e+03	3.697e-09	8.157e+04	2.070e-13
5.669e-03	2.317e-01	3.577e-01	4.429e-01	2.257e+01	1.647e-04	1.424e+03	2.933e-09	8.983e+04	1.651e-13
6.242e-03	2.482e-01	3.938e-01	4.159e-01	2.485e+01	1.267e-04	1.568e+03	2.327e-09	9.892e+04	1.317e-13
6.874e-03	2.657e-01	4.337e-01	3.881e-01	2.736e+01	9.724e-05	1.726e+03	1.847e-09
7.569e-03	2.842e-01	4.776e-01	3.598e-01	3.013e+01	7.456e-05	1.901e+03	1.466e-09
8.335e-03	3.038e-01	5.259e-01	3.314e-01	3.318e+01	5.711e-05	2.093e+03	1.165e-09
9.179e-03	3.244e-01	5.791e-01	3.034e-01	3.654e+01	4.370e-05	2.305e+03	9.252e-10
1.011e-02	3.461e-01	6.377e-01	2.762e-01	4.023e+01	3.340e-05	2.539e+03	7.352e-10
1.113e-02	3.689e-01	7.022e-01	2.504e-01	4.431e+01	2.551e-05	2.795e+03	5.844e-10
1.226e-02	3.928e-01	7.733e-01	2.267e-01	4.879e+01	1.947e-05	3.078e+03	4.646e-10
1.350e-02	4.176e-01	8.515e-01	2.050e-01	5.373e+01	1.485e-05	3.390e+03	3.695e-10
1.486e-02	4.435e-01	9.377e-01	1.853e-01	5.916e+01	1.131e-05	3.733e+03	2.939e-10
1.637e-02	4.701e-01	1.033e+00	1.674e-01	6.515e+01	8.619e-06	4.110e+03	2.338e-10
1.802e-02	4.970e-01	1.137e+00	1.503e-01	7.174e+01	6.565e-06	4.526e+03	1.861e-10
1.985e-02	5.238e-01	1.252e+00	1.321e-01	7.900e+01	5.001e-06	4.984e+03	1.481e-10
2.185e-02	5.495e-01	1.379e+00	1.124e-01	8.699e+01	3.811e-06	5.489e+03	1.179e-10
2.406e-02	5.741e-01	1.518e+00	9.378e-02	9.580e+01	2.906e-06	6.044e+03	9.387e-11
2.650e-02	5.972e-01	1.672e+00	7.750e-02	1.055e+02	2.217e-06	6.656e+03	7.475e-11
2.918e-02	6.186e-01	1.841e+00	6.368e-02	1.162e+02	1.694e-06	7.329e+03	5.953e-11
3.213e-02	6.380e-01	2.027e+00	5.215e-02	1.279e+02	1.296e-06	8.071e+03	4.742e-11
3.539e-02	6.553e-01	2.233e+00	4.269e-02	1.409e+02	9.936e-07	8.887e+03	3.778e-11

Note. Differential intensity units: $(m^2 \text{ s sr GeV n}^{-1})^{-1}$.

(This table is available in machine-readable form.)

ORCID iDs

- M. J. Boschini [DOI](https://orcid.org/0000-0002-6401-0457) <https://orcid.org/0000-0002-6401-0457>
 S. Della Torre [DOI](https://orcid.org/0000-0002-7669-0859) <https://orcid.org/0000-0002-7669-0859>
 M. Gervasi [DOI](https://orcid.org/0000-0003-3884-0905) <https://orcid.org/0000-0003-3884-0905>
 D. Grandi [DOI](https://orcid.org/0000-0003-1942-8587) <https://orcid.org/0000-0003-1942-8587>
 G. Jóhannesson [DOI](https://orcid.org/0000-0003-1458-7036) <https://orcid.org/0000-0003-1458-7036>
 G. La Vacca [DOI](https://orcid.org/0000-0002-2168-9447) <https://orcid.org/0000-0002-2168-9447>
 N. Masi [DOI](https://orcid.org/0000-0002-3729-7608) <https://orcid.org/0000-0002-3729-7608>
 I. V. Moskalenko [DOI](https://orcid.org/0000-0001-6141-458X) <https://orcid.org/0000-0001-6141-458X>
 T. A. Porter [DOI](https://orcid.org/0000-0002-2621-4440) <https://orcid.org/0000-0002-2621-4440>
 P. G. Rancoita [DOI](https://orcid.org/0000-0002-1990-4283) <https://orcid.org/0000-0002-1990-4283>
 D. Rozza [DOI](https://orcid.org/0000-0002-7378-6353) <https://orcid.org/0000-0002-7378-6353>
 M. Tacconi [DOI](https://orcid.org/0000-0002-9344-6305) <https://orcid.org/0000-0002-9344-6305>

References

- Aguilar, M., Aisa, D., Alpat, B., et al. 2014, *PhRvL*, **113**, 221102
 Aguilar, M., Aisa, D., Alpat, B., et al. 2015a, *PhRvL*, **114**, 171103
 Aguilar, M., Aisa, D., Alpat, B., et al. 2015b, *PhRvL*, **115**, 211101
 Aguilar, M., Ali Cavasonza, L., Alpat, B., et al. 2016a, *PhRvL*, **117**, 091103
 Aguilar, M., Ali Cavasonza, L., Alpat, B., et al. 2017, *PhRvL*, **119**, 251101
 Aguilar, M., Ali Cavasonza, L., Alpat, B., et al. 2018a, *PhRvL*, **121**, 051103
 Aguilar, M., Ali Cavasonza, L., Alpat, B., et al. 2019a, *PhRvL*, **122**, 101101
 Aguilar, M., Ali Cavasonza, L., Ambrosi, G., et al. 2016b, *PhRvL*, **117**, 231102
 Aguilar, M., Ali Cavasonza, L., Ambrosi, G., et al. 2018b, *PhRvL*, **120**, 021101
 Aguilar, M., Ali Cavasonza, L., Ambrosi, G., et al. 2019b, *PhRvL*, **122**, 041102
 Aguilar, M., Ali Cavasonza, L., Ambrosi, G., et al. 2020, *PhRvL*, **124**, 211102
 Aguilar, M., Ali Cavasonza, L., Ambrosi, G., et al. 2021a, *PhR*, **894**, 1
 Aguilar, M., Ali Cavasonza, L., Allen, M. S., et al. 2021b, *PhRvL*, **126**, 081102
 Aguilar, M., Ali Cavasonza, L., Allen, M. S., et al. 2021c, *PhRvL*, **126**, 041104
 Aguilar, M., Ali Cavasonza, L., Alpat, B., et al. 2021d, *PhRvL*, **127**, 021101
 Ahn, H. S., Allison, P., Bagliesi, M. G., et al. 2009, *ApJ*, **707**, 593
 Ahn, H. S., Allison, P. S., Bagliesi, M. G., et al. 2008, *APh*, **30**, 133
 Artun, O., Cassagnou, Y., Legrain, R., et al. 1975, *PhRvL*, **35**, 773
 Barashenkov, V. S., & Polanski, A. 1994, Electronic Guide for Nuclear Cross Sections, Technical Report, E2-94-417, CERN
 Bauhoff, W. 1986, *ADNDT*, **35**, 429
 Berezhinskii, V. S., Bulanov, S. V., Dogiel, V. A., & Ptuskin, V. S. 1990, in *Astrophysics of Cosmic Rays*, ed. V. L. Ginzburg (North-Holland, Amsterdam)
 Binns, W. R., Israel, M. H., Christian, E. R., et al. 2016, *Sci*, **352**, 677
 Binns, W. R., Wiedenbeck, M. E., Arnould, M., et al. 2008, *NewAR*, **52**, 427
 Bobchenko, B. M., Buklei, A. E., Vlasov, A. V., et al. 1979, *SvJNP*, **30**, 805
 Bobik, P., Boschini, M. J., Della Torre, S., et al. 2016, *JGRA*, **121**, 3920
 Boschini, M. J., Della Torre, S., Gervasi, M., et al. 2017, *ApJ*, **840**, 115
 Boschini, M. J., Della Torre, S., Gervasi, M., et al. 2018a, *ApJ*, **854**, 94
 Boschini, M. J., Della Torre, S., Gervasi, M., et al. 2018b, *ApJ*, **858**, 61
 Boschini, M. J., Della Torre, S., Gervasi, M., et al. 2020a, *ApJS*, **250**, 27
 Boschini, M. J., Della Torre, S., Gervasi, M., et al. 2020b, *ApJ*, **889**, 167
 Boschini, M. J., Della Torre, S., Gervasi, M., et al. 2021, *ApJ*, **913**, 5
 Boschini, M. J., Della Torre, S., Gervasi, M., et al. 2022, *ApJ*, **925**, 108
 Boschini, M. J., Della Torre, S., Gervasi, M., La Vacca, G., & Rancoita, P. G. 2019, *AdSpR*, **64**, 2459
 Bouchet, L., Jourdain, E., & Roques, J.-P. 2015, *ApJ*, **801**, 142
 Cummings, A. C., Stone, E. C., Heikkila, B. C., et al. 2016, *ApJ*, **831**, 18
 Di Felice, V., Pizzolotto, C., D'Urso, D., et al. 2017, *ICRC (Busan)*, **301**, 1073
 Diehl, R., Dupraz, C., Bennett, K., et al. 1995, *A&A*, **298**, 445
 Diehl, R., Halloin, H., Kretschmer, K., et al. 2006, *Natur*, **439**, 45
 Diehl, R., Lugaro, M., Heger, A., et al. 2021, *PASA*, **38**, e062
 Engelmann, J. J., Ferrando, P., Soutoul, A., et al. 1990, *A&A*, **233**, 96
 Goswami, J. N., Marhas, K. K., Chaussidon, M., Gounelle, M., & Meyer, B. S. 2005, in *ASP Conf. Ser.* 341, Chondrites and the Protoplanetary Disk, ed. A. N. Krot, E. R. D. Scott, & B. Reipurth (San Francisco, CA: ASP), **485**
 Grebenyuk, V., Karmanov, D., Kovalev, I., et al. 2019, *AdSpR*, **64**, 2559
 Hirzebruch, S. E., Heinrich, W., Tolstov, K. D., & Kovalenko, A. D. 1991, *Proc. ICRC (Dublin)*, **2**, 280
 Knöldeseder, J., Dixon, D., Bennett, K., et al. 1999, *A&A*, **345**, 813
 Lave, K. A., Wiedenbeck, M. E., Binns, W. R., et al. 2013, *ApJ*, **770**, 117
 Lukasiak, A. M., McDonald, F. B., & Webber, W. R. 1994, *ApJL*, **430**, L69
 Malkov, M. A., & Drury, L. O. 2001, *RPPh*, **64**, 429
 Maurin, D., Melot, F., & Taillet, R. 2014, *A&A*, **569**, A32
 Moskalenko, I. V., Mashnik, S. G., & Strong, A. W. 2001, *ICRC (Hamburg)*, **5**, 1836
 Moskalenko, I. V., Strong, A. W., & Mashnik, S. G. 2005, in *AIP Conf. Ser.* 769, Int. Conf. on Nuclear Data for Science and Technology, ed. R. C. Haight et al. (Melville, NY: AIP), 1612
 Moskalenko, I. V., Vladimirov, A. E., Porter, T. A., & Strong, A. W. 2013, *ICRC (Rio de Janeiro)*, **33**, 0823
 Oberlack, U., Bennett, K., Bloemen, H., et al. 1996, *A&AS*, **120**, 311
 Panov, A. D., Adams, J. H., Ahn, H. S., et al. 2009, *BRASP*, **73**, 564
 Porter, T. A., Johannesson, G., & Moskalenko, I. V. 2021, arXiv:**2112.12745**
 Prantzos, N., & Diehl, R. 1996, *PhR*, **267**, 1
 Seo, E. S., & Ptuskin, V. S. 1994, *ApJ*, **431**, 705
 Simpson, J. A., & Connell, J. J. 1998, *ApJL*, **497**, L85
 Smiljanic, R., Romano, D., Bragaglia, A., et al. 2016, *A&A*, **589**, A115
 Strong, A. W., Moskalenko, I. V., & Ptuskin, V. S. 2007, *ARNPS*, **57**, 285
 Vladimirov, A. E., Johannesson, G., Moskalenko, I. V., & Porter, T. A. 2012, *ApJ*, **752**, 68
 Webber, W. R. 1982, *ApJ*, **252**, 386
 Webber, W. R., Kish, J. C., & Schrier, D. A. 1990, *PhRvC*, **41**, 547
 Webber, W. R., Soutoul, A., Kish, J. C., et al. 1998, *PhRvC*, **58**, 3539
 Webber, W. R., Soutoul, A., Kish, J. C., & Rockstroh, J. M. 2003, *ApJS*, **144**, 153
 Wellisch, H. P., & Axen, D. 1996, *PhRvC*, **54**, 1329
 Wiedenbeck, M. E. 1983, *ICRC (Bangalore)*, **9**, 147
 Yanasak, N. E., Wiedenbeck, M. E., Mewaldt, R. A., et al. 2001, *ApJ*, **563**, 768